CHALMERS
UNIVERSITY OF TECHNOLOGY

CFD methods for liquid mixing with the presence of a vortex

A comparative study of simulational methods with experimental validation

Master's thesis in Applied Mechanics

JACOB LARSSON
LISA LINDENBAUM

DEPARTMENT OF MECHANICAL AND MARITIME SCIENCES
CHALMERS UNIVERSITY OF TECHNOLOGY
Gothenburg, Sweden 2023
www.chalmers.se

Master's thesis 2023

CFD methods for liquid mixing with the presence of a vortex

A comparative study of simulational methods with experimental validation

JACOB LARSSON
LISA LINDENBAUM

CHALMERS
UNIVERSITY OF TECHNOLOGY

Department of Mechanical and Maritime Sciences
Division of Fluid Dynamics
Chalmers University of Technology
Gothenburg, Sweden 2023

CFD methods for liquid mixing with the presence of a vortex
Comparative study of simulational methods with experimental validation

JACOB LARSSON
LISA LINDENBAUM

Master's Thesis 2023
Department of Mechanical and Maritime Sciences
Division of Fluid Dynamics
Chalmers University of Technology
SE-412 96 Gothenburg
Sweden
Telephone +46 31 772 1000

Cover: Visualization of the transportation of the tracer liquid represented as a passive scalar. Generated with Blender.

Printed by Chalmers Reproservice
Gothenburg, Sweden 2023

CFD methods for liquid mixing with the presence of a vortex
A comparative study of simulational methods with experimental validation
JACOB LARSSON
LISA LINDENBAUM
Department of Mechanical and Maritime Sciences
Chalmers University of Technology

Abstract

Mixing liquids is a fundamental process in many industrial and laboratory applications, extensively studied through experimental and numerical approaches. Obtaining certain information through experiments can however be challenging and expensive, while easily obtained through simulations with Computational Fluid Dynamics (CFD). It is therefore of interest to identify cost-effective CFD methods for accurate mixing prediction. This thesis will further investigate practices when simulating stirred tanks in CFD by focusing on effects that appear with the presence of a vortex. Through simulations and experiments, power number, pumping number, and mixing time are determined and analysed. This is done at different operational conditions with and without a vortex. The stirred tank is simulated both as steady state and with the free surface fixed and as unsteady with the free surface being solved at operational conditions with a vortex present.

Treating the flow as steady and neglecting the vortex is found to have a minor impact on power number, pumping number, and mixing time, while significantly reducing computational costs. However, the presence of a vortex affects the fluid's velocity field, thus also affecting the transportation of the species that is to be mixed. The flow is therefore to be treated as unsteady and the free surface should be solved in order to accurately predict the transient mixing behaviour. Both the steady and transient approach correspond well with experiments over all, but at operational conditions with vortex, both methods overestimate mixing time by up to 30%.

The results indicate that the power number, pumping number, and dimensionless mixing time are independent of Reynolds number under fully turbulent conditions. Changing the water level in the tank, leading to the presence of a vortex, has a minor impact on the pumping number but a significant effect on the others. Estimation of the mixing time based on the pumping number and water volume yields consistent results across varying water levels, making it especially practical due to the limited variation of pumping number.

Keywords: CFD, Eccentric agitation, Stirred tank, Power number, Pumping number, Mixing, Free-surface, Vortex

Acknowledgements

We want to give a huge thanks to our supervisor, Robert Rundqvist, for sharing his knowledge and guidance with us throughout our project. His expertise and support were instrumental in helping us to achieve our objectives and complete our thesis successfully. We are grateful for all his time and effort, and we could not have done it without him.

We would also like to extend a thank you to Johan Nordberg at Metenova for his assistance during our experiments. His technical expertise and support were indispensable in ensuring the accuracy and reliability of our data.

Furthermore a thanks goes out to our examiner at Chalmers, Henrik Ström, for being our examiner and ensuring that the work continued smoothly. Additionally, to conclude our time at Chalmers with the same examiner we had in our first course feels like a perfect way to tie everything together.

Finally, we would like to thank all the employees at FS Dynamics for making us feel welcome and made our work there enjoyable.

Jacob Larsson and Lisa Lindenbaum, Gothenburg, June 2023

List of Acronyms

Below is the list of acronyms that have been used throughout this thesis listed in alphabetical order:

CAD	Computed Aided Design
CPU	Central Processing Unit
CFD	Computational Fluid Dynamics
DES	Detached Eddy Simulation
DNS	Direct Numerical Simulation
MRF	Multiple Reference Frame
LES	Large Eddy Simulation
RANS	Reynolds Average Navier Stokes
RSM	Reynolds Stress Model
SM	Sliding Mesh
SST	Shear Stress Transport
VOF	Volume of Fluids

Nomenclature

Greek letters

α_{VOF}	Volume fraction	[-]
α_{EB}	Elliptic blending coefficient	[-]
β, β^*	Turbulence modeling constants	[-]
δ_{ij}	Kronecker delta	[-]
ε	Turbulent dissipation rate	[m^2/s^3]
η	Component of turbulent anisotropy	[-]
θ_{95}	Dimensionless mixing time for 95% mixing	[-]
λ	Turbulent Taylor length scale	[m]
μ	Dynamic viscosity	[Pa s]
ν	Kinematic viscosity	[m^2/s]
ν_t	Turbulent kinematic viscosity	[m^2/s]
Π_{ij}	Pressure strain tensor	[m^2/s^3]
ρ	Density	[kg/m^3]
σ_k, σ_ε, σ_ω	Turbulent Prandtl number	[-]
τ	Torque	[N m]
τ_{95}	Mixing time for 95% mixing	[s]
ϕ	Passive scalar	[-]
ω	Specific dissipation rate	[1/s]

Roman letters

c_t	Concentration of tracer fluid	[-]
c_T, $c_{\varepsilon 1}$, $c_{\varepsilon 2}$, c_μ	Turbulence modeling constants	[-]
CV	Coefficient of Variance	[-]
D	Diameter	[m]
k	Turbulent kinetic energy	[m^2/s^2]
l_0	Turbulent integral length scale	[m]
N	Rotational speed	[rps]

N_P	Power number	[-]
N_Q	Pumping number	[-]
P	Power	[N m/s]
P_ε	Production term in transport of ε	[m]
P_ω	Production term in transport of ω	[m]
P_k	Production term in transport of k	[m]
Q	Volumetric flow rate	[m^3/s]
R_{ij}	Reynolds stress tensor	[N/m^2]
Re	Reynolds number	[-]
s_{ij}	Strain rate tensor	[1/s]
Sc	Schmidt number	[-]
Sc_t	Turbulent Schmidt number	[-]
t	Time	[s]
u^*	Frictional velocity	[m/s]
v_i	Velocity tensor	[m/s]
V	Tank volume	[m^3]
ΔV	Cell volume	[m^3]
x_i	Coordinate tensor	[m]
Δx	Cell length	[m]
y	Wall distance	[m]
y^+	Dimensionless wall distance	[-]

Averaging notations

$\langle\Phi\rangle$	Temporal average
Φ'	Temporal fluctuation
$\overline{\Phi}$	Spatial average
Φ''	Spatial fluctuation

Contents

1 Introduction

The mixing of different liquids is a fundamental process in numerous industrial and laboratory applications, including food and beverage production, chemical production, and pharmaceutical manufacturing. One common method for mixing liquids involves using an impeller that generates a moving flow by rotating within a tank. Studying the mixing process provides valuable knowledge on how to optimize the design of the tank and impeller, thus increasing the efficiency of the factory. However, experimentation can be costly and challenging to perform, making it beneficial to use Computational Fluid Dynamics (CFD) to gain a deeper understanding of the mixing process.

Mixing is performed with different volumes and impeller speeds, leading to varying behaviors in the liquid. Tanks used for mixing often contain baffles that prevent the swirling motion of the liquid and keep a a vortex from forming. In cases where no baffles are included a vortex is commonly formed when the liquid level is high compared to the tank diameter. A vortex distinctly affects the flow field of the liquid. Turbulence is another crucial aspect of mixing in a tank as it greatly influences the flow patterns and mixing efficiency.

1.1 Background

Mixing in stirred tanks has been extensively studied using both experimental and numerical methods. However, the majority of the work has focused on mixing with a center-mounted Rushton turbine or similar impeller in closed tanks with baffles, assuming a fixed water surface. The Rushton turbine is a radial flow impeller that consists of a horizontal disc with vertical blades mounted on the disc. Literature considering a free surface with a water-air interface and an eccentrically mounted impeller is scarce. A literature review was conducted to create an overview of previous work and determine which methods are suitable for different approaches.

Several methods exist to represent the rotation of the impeller, and their suitability depends on the application and desired information from the simulation. The two most common models are the Multiple Reference Frame (MRF) and Sliding Mesh (SM). The MRF model is a steady-state approach and is suitable when the flow in the vicinity of the impeller has weak coupling to the bulk fluid in the tank and can be assumed to be time-independent with respect to the impeller. It has been shown that overall, the MRF technique models the mean flow patterns well for an

impeller mounted in the center of a tank [1]. The SM model is a transient method of modeling the rotation, where the region that contains the impeller is rotated with the impeller, causing a periodic time-dependent flow. CFD simulations using a six-bladed Rushton turbine with an eccentric configuration showed that steady-state simulations should be avoided since they caused nonphysical swirls in the flow when the interaction between the impeller jet and walls was significant [2].

The most commonly used approach for modeling turbulence is the Reynolds-averaged Navier-Stokes (RANS) turbulence model. In the case of stirred tanks, most of the research on RANS turbulence models have focused on simpler two-equation models that assume isotropic turbulence. These models generally provide good predictions of the velocity field but tend to underestimate turbulent energy and overestimate mixing time [3]. Turbulence models that account for anisotropic turbulence, such as the Reynolds Stress Model (RSM), require significantly more computational resources than simpler models and are generally not used in simulations with a fixed water surface. However, it has been shown that considering the anisotropy of turbulence provides additional accuracy when modeling the free surface in stirred tanks with swirling flow [4][5][6].

The turbulence modeling approach that has shown the best results in previous work is the Large Eddy Simulation (LES), which solves large scale turbulence and models small scales. This approach has in several cases shown results closer to experimental data than RANS [7][8]. The drawback of LES is however that a much finer mesh is needed compared to RANS in order to resolve the large turbulent structures, particularly near walls. In recent years there has also been a limited amount of work done by using Detached Eddy Simulation (DES) which combines RANS and LES by utilizing the strength of each model, using RANS close to walls which provides decent accuracy together with low computational cost and using LES in the free flow where RANS models tend to struggle. An implementation of DES in a simulation of an eccentric impeller in a stirred tank predicted mixing times that were overestimated by 20% compared to experimental data [9], which is seen as a good result since over predictions are typically even larger with two equation RANS models.

Graeme L. Lane investigated CFD modeling methods for a hydrofoil impeller and concluded that the models that have given good results for a Rushton turbine are not suitable for this type of impeller, for example, standard $k-\varepsilon$ turbulence model performed quite poorly [10].

Modeling of the free surface between liquid and gas in stirred tanks is most commonly done with Volume of Fluid (VOF). Simulations with free surface modeling are often treated as a transient case, but work has still been done by using time averaging models and methods such as RANS and MRF in transient simulations. For a central magnetic impeller, Mahmud et al. showed that using VOF with a combination of RANS and MRF generated reasonable results however with an underestimation of the depth of the vortex [4]. The work also showed that the turbulence was largely isotropic in the bulk flow, and similar results were thus obtained with the SST $k-\omega$

model and the Reynolds Stress Model (RSM). For an eccentric mounted Rushton turbine in an unbaffled tank, Yang et al. achieved a good correlation with experimental data in terms of velocity measurements when solving the free surface with VOF and DES [11].

1.2 Purpose and objective

This thesis will further investigate the practices of simulating the free surface in a stirred tank with an eccentric impeller by evaluating methods based on literature, simulations and testing. This will be done by studying a stirred tank configuration at different operational conditions both with and without a vortex and fulfilling the following objectives.

- Perform experiments at Metenova and obtain power number and mixing time.
- Perform CFD simulations and obtain power number, pumping number and mixing time.
- Evaluate methods used in CFD based on comparison of results with the experiment.
- Evaluate the current rules for predicting the mixing time and propose changes if necessary.

1.3 Demarcations

The thesis is conducted with the following demarcations.

- One geometrical setup with tank and impeller is used to simulate four operational conditions with different rotational speed of the impeller and water height.
- All cases are assumed to be fully turbulent. The dimensionless numbers are therefore independent of Reynolds number.
- All cases are simulated with modeled turbulence. The use of turbulence resolving methods will be limited to substantiate the choice of turbulence model.
- Operational conditions where a vortex is not present are simulated with a slip wall as a representation of the water surface.
- The mixing process considers mixing of saline in water. The saline is assumed to have the same properties as the water.

1.4 Societal, ethical and ecological aspects

To create vaccines, liquids containing different bacteria often need to be mixed. During the last years with the Covid-19 pandemic, there has been an extreme need to be able to produce large quantities of vaccines. Because of the uncertainties about mixing times, companies tend to let "overmix" the vaccine since the vaccines must be well blended. If more reliable mixing times can be computed with the help of CFD, the mixing time can be reduced which would mean that the total time of creating a vaccine can be reduced. Shortened manufacturing time leads to a reduced cost per dose and that, if there is a need, it would be possible to reach large parts of the population more quickly. This is also good from an environmental point of view as energy consumption would be reduced.

However, it is also important to consider the potential negative impacts of this research. The use of CFD simulations can save time and resources compared to experimental methods, but the use of simulations in the industry should be done with caution. The results of simulations must be validated by experimental data and it is important to ensure that the simulation accurately represents the real-world process. If the calculated mixing time turns out to be incorrect, this would have disastrous consequences as it could lead to ineffective vaccines.

2 Theory

The theory chapter starts by explaining some important concepts regarding agitated tanks, and how to calculate these. Thereafter follow theory about CFD, including turbulence models, VOF, passive scalar and moving bodies.

2.1 Industrial mixing

Mixing in stirred tanks as investigated in this thesis is accomplished by inducing motion to two fluids through an impeller in the tank. In this thesis, the impeller is a bottom mounted mixed flow impeller. It allows the flow to enter the impeller from the axial direction and then be deflected in radial direction when it is pushed out at the bottom of the tank, creating circulation in the tank. Impeller and tank configurations are often evaluated using characteristic dimensionless numbers such as power number, pumping number and dimensionless mixing time.

These numbers are often found to be independent of Reynolds number in fully turbulent conditions, when the inertial forces of the fluid become dominant over the viscous forces. The transition to fully turbulent flow in stirred tanks usually occurs within the range of $50 < Re < 5000$ [12]. The Reynolds number in a stirred tank is commonly defined, as in equation (2.1), based on the impeller diameter D, rotational speed N, along with the density ρ and dynamic viscosity μ of the fluid being mixed.

$$Re = \frac{\rho N D^2}{\mu} \tag{2.1}$$

2.1.1 Power number

The power number is a non-dimensional measure of the power exerted on the fluid by the impeller. The power number can be calculated in two ways: either using the torque of the impeller or the volume integral of the dissipation rate of turbulent kinetic energy. Since there is no energy extracted from the tank, the power from the impeller must be dissipated. The power number based on torque is calculates as

$$N_{P,\tau} = \frac{P}{\rho N^3 D^5} \quad , P = 2\pi N \tau \tag{2.2}$$

where the power P is calculated based on τ which is the torque of the impeller. The power number based on dissipation rate of turbulent kinetic energy, ε, is determined as

$$N_{P,\varepsilon} = \frac{\int_V \rho\varepsilon \, dV}{\rho N^3 D^5}. \tag{2.3}$$

Using the dissipation rate have however been found to underestimate the power number for the most common turbulence models, while the results of the torque agree well with experiments [13].

2.1.2 Pumping number

The pumping number, also called flow number, is a measure of the volumetric flow rate, Q, through the impeller that is made non-dimensional with the rotational speed and diameter of the impeller. It is defined as

$$N_Q = \frac{Q}{ND^3}. \tag{2.4}$$

The pumping number can therefore be used as a measurement of how well the impeller moves the fluid.

2.1.3 Mixing time

The mixing time is the time required to reach a certain homogeneity of the mixture. It can be defined in different ways, based on both local and global measurements. Mixing based on local measurements is suitable for experiments where the concentration of a species can be measured at one or several points. The mixing time can then be determined by the time it takes for the measured concentration, c_t, to stabilize within a certain range of the average concentration in the tank, $\bar{c_t}$. To achieve a desired level of homogeneity at 95 % or above, the following criteria should be achieved at the measuring point.

$$0.95 < \frac{c_t}{\bar{c_t}} < 1.05 \tag{2.5}$$

A global definition of the mixing time is suitable for use with results from CFD since measurements can be taken in the whole domain. The mixing time is then defined as the time it takes to reach a certain value of the coefficient of variance (CV), which corresponds to the desired level of homogeneity. The coefficient of variance is defined as the ratio of the standard deviation to the mean:

$$CV = \sqrt{\frac{\int_V \left(\frac{c_t(\mathbf{x}) - \bar{c_t}}{\bar{c_t}}\right)^2 dV}{V}} \tag{2.6}$$

which can be discretized as

$$CV = \sqrt{\frac{\sum_i^n \left(\frac{c_{t,i} - \bar{c_t}}{\bar{c_t}}\right)^2 \Delta V_i}{\sum_i^n \Delta V_i}} \tag{2.7}$$

where the summation is done over the cells in the domain and ΔV_i is the volume of cell i. The threshold value of CV in order to obtain a certain mixture is through a statistical experiment by Hartmann et al. [8] found to be

$$CV = 0.17\left(\frac{100 - c_{\%}}{30}\right). \tag{2.8}$$

A mixing with $c_{\%} = 95$ gives $CV = 0.0283$.

The mixing time, τ_{95}, is often made dimensionless by multiplication with the rotational speed of the impeller.

$$\theta_{95} = N\tau_{95} \tag{2.9}$$

The dimensionless mixing time is typically independent of the Reynolds number in fully turbulent flow and can therefore be used to predict mixing time with changing impeller speed. However, the dimensionless mixing time does not account for changing liquid volume. Therefore, a rule of thumb is used in the industry to estimate the mixing time.According to this rule, it takes approximately four to five turnover times to achieve a homogeneity of 95 %. The turnover time is defined as the time it takes for the total liquid volume in the tank to pass through the impeller. This estimation is however only useful if the volumetric flow rate of the impeller, or the pumping number, is known. In such case the estimated mixing time can be calculated as $5V/Q$ or $5V/(ND^3N_Q)$.

2.2 Computational fluid dynamics

In computational fluid dynamics (CFD) the solution of the flow field is commonly obtained by solving the governing equations of the flow in the Eulerian reference frame. For a closed system without heat sources, these equations are the conservation of mass and momentum, known as the Navier-Stokes equations. Since the studied fluids are liquids and air at low velocities, they are considered incompressible. The conservation of mass is defined as shown in equation (2.10) with velocity tensor v_i and the positional tensor x_i, where i denotes direction in the Cartesian coordinate system.

$$\frac{\partial v_i}{\partial x_i} = 0 \tag{2.10}$$

The conservation of momentum is defined as shown in equation (2.11), where t is the time p is the pressure, μ is the dynamic viscosity, δ_{ij} is the Kronecker delta, and f_i represents body forces [14].

$$\frac{\partial v_i}{\partial t} + \frac{\partial v_i v_j}{\partial x_j} = -\frac{1}{\rho}\frac{\partial p}{\partial x_i} + \frac{\partial}{\partial x_j}\left[\nu\left(\frac{\partial v_i}{\partial x_j} + \frac{\partial v_j}{\partial x_i}\right) - \frac{2}{3}\nu\frac{\partial v_k}{\partial x_k}\delta_{ij}\right] + f_i \tag{2.11}$$

2.2.1 Reynolds-Averaged Navier-Stokes equations

Turbulent flows are more complex than laminar flows, characterized by their chaotic fluctuations in space and time. To address this complexity, the Navier-Stokes equa-

tions are often time averaged. The instantaneous properties of the flow are decomposed into a mean, time averaged, value, and a fluctuating value

$$\Phi = \langle \Phi \rangle + \Phi' \tag{2.12}$$

where the time averaged value is defined as

$$\langle \Phi \rangle = \frac{1}{2T} \int_{-T}^{T} \Phi(t)\, dt. \tag{2.13}$$

Introducing the decomposition in Navier-Stokes equations yields

$$\frac{\partial \langle v_i \rangle}{\partial x_i} = 0 \tag{2.14}$$

$$\begin{aligned} \frac{\partial \langle v_i \rangle}{\partial t} + \frac{\partial \langle v_i \rangle \langle v_j \rangle}{\partial x_j} = &- \frac{1}{\rho} \frac{\partial \langle p \rangle}{\partial x_i} + \frac{\partial}{\partial x_j} \left[\nu \left(\frac{\partial \langle v_i \rangle}{\partial x_j} + \frac{\partial \langle v_j \rangle}{\partial x_i} \right) \right. \\ &\left. - \frac{2}{3} \nu \frac{\partial \langle v_k \rangle}{\partial x_k} \delta_{ij} - \langle v_i' v_j' \rangle \right] + f_i. \end{aligned} \tag{2.15}$$

The new term, $\langle v_i' v_j' \rangle$, is used to calculate the Reynolds stress tensor $R_{ij} = \rho \langle v_i' v_j' \rangle$ and represents the correlation between the fluctuating velocities. This stress term is due to turbulence and needs to be either solved or modeled to close equation (2.15)[14].

2.2.2 RANS based turbulence models

The purpose of RANS-based turbulence models is to solve or model the Reynolds stresses from the momentum equation in order to close equation (2.15). A distinct difference between turbulence models is whether the Reynolds stresses are assumed to be isotropic or not. In models assuming isotropic turbulence, a commonly used method is to employ an eddy viscosity model, where the turbulent stresses are related to the mean flow by introducing a proportionality constant ν_t. The most common model is the Boussinesq assumption

$$\langle v_i' v_j' \rangle = -2\nu_t \langle s_{ij} \rangle + \frac{2}{3} k \delta_{ij} \tag{2.16}$$

where ν_t is the turbulent eddy viscosity, $\langle s_{ij} \rangle = \frac{1}{2}(\frac{\partial \langle v_i \rangle}{\partial x_j} + \frac{\partial \langle v_j \rangle}{\partial x_i})$ is the mean strain rate tensor, and $k = \frac{1}{2}\langle v_i' v_i' \rangle$ is the turbulent kinetic energy. By inserting equation (2.16) into equation (2.15), the six unknown turbulent stresses are replaced with a single unknown.

Turbulence models that solves all Reynolds stresses allow for analysis that can determine the type of turbulence that is present in different regions of the flow. The anisotropic tensor can be calculated from the Reynolds stress tensor by subtracting the normal stresses with the average normal stress. The normalized anisotropic tensor B_{ij}, is then used to analyze the characteristics of the turbulence.

$$B_{ij} = \frac{R_{ij}/\rho}{2k} - \frac{1}{3}\delta_{ij} \tag{2.17}$$

The second invariant, I_2, of the anisotropic tensor is used to calculate η, which can be regarded as a measure of isotropy in the turbulence.

$$\eta = \sqrt{-\frac{1}{3}I_2} \tag{2.18}$$

The range of η is $0 \leq \eta \leq 1/3$ where $\eta = 0$ indicates fully isotropic turbulence, and an increase of η indicates more anisotropy.

2.2.2.1 $k - \varepsilon$ model

The $k - \varepsilon$ is the most widely used model for industrial applications to determine the turbulent eddy viscosity. The model is known to be robust and is the most commonly used RANS model in mixing applications [3]. The model is based on two transport equations, the modeled turbulent kinetic energy (k) in equation (2.19) and the modeled turbulent dissipation rate (ε) in equation (2.20).

$$\frac{\partial k}{\partial t} + \frac{\partial}{\partial x_j}(\langle v_j \rangle k) = P_k + \frac{\partial}{\partial x_j}\left[\left(\nu + \frac{\nu_t}{\sigma_k}\right)\frac{\partial k}{\partial x_j}\right] - \varepsilon \tag{2.19}$$

$$\frac{\partial \varepsilon}{\partial t} + \frac{\partial}{\partial x_j}(\langle v_j \rangle \varepsilon) = \frac{\varepsilon}{k} c_{\varepsilon 1} \nu_t P_\varepsilon + \frac{\partial}{\partial x_j}\left[\left(\nu + \frac{\nu_t}{\sigma_\varepsilon}\right)\frac{\partial \varepsilon}{\partial x_j}\right] - c_{\varepsilon 2} f_2 \frac{\varepsilon^2}{k} \tag{2.20}$$

The turbulent viscosity is then calculated as following

$$\nu_t = c_\mu f_\mu \frac{k^2}{\varepsilon}. \tag{2.21}$$

The values of the coefficients σ_k, σ_ε, $c_{\varepsilon 1}$, $c_{\varepsilon 2}$ and c_μ as well as the definition of the damping functions f_2, f_μ and production terms P_k and P_ε varies between different versions of the $k - \varepsilon$ model and can be found in the Simcenter STAR-CCM+ documentation [15]. The standard $k - \varepsilon$ model does not implement damping on the turbulent viscosity and transport of turbulent dissipation rate, the damping are hence fixed at unity.

2.2.2.2 Realizable $k - \varepsilon$ model

According to the Boussinesq assumption, the normal stresses of a fluid element are related to the normal strain in equation (2.16). Large normal strain can thus generate nonphysical negative normal stresses, which may lead to an overproduction of the turbulent viscosity. The turbulent viscosity is limited in the realizable $k - \varepsilon$ model by relating the damping function f_μ to the strain tensor and its principle values. By limiting the turbulent viscosity in such a way that the normal stress are positive in the principle direction of the strain, ensures that the normal stresses remain positive regardless of rotation.

Furthermore, the realizable $k - \varepsilon$ model implements a modified transport equation for the modeled turbulent dissipation rate, as proposed by Shih et al. [16]. This modified transport equation is based on the transport equation for the modeled mean-square vorticity fluctuation $\langle \omega_i \omega_i \rangle$ and then using the relation $\varepsilon = \nu \langle \omega_i \omega_i \rangle$. The transition from the standard equation to the modified one is handled through the damping factor f_2.

2.2.2.3 SST $k-\omega$ model

The SST $k-\omega$ model is another two-equation eddy viscosity model that combines the $k-\varepsilon$ and $k-\omega$ models. The $k-\omega$ model tends to perform better close to walls without the need for damping functions, while $k-\varepsilon$ is more robust in free-stream flow. The model is derived by expressing the transport of ε in equation (2.20) in terms of the specific dissipation rate (ω) by using the relation $\omega \propto \varepsilon/k$, resulting in equation (2.22). The transport of k in equation (2.19) is modified by substituting ε with $\beta^* k\omega$, resulting in equation (2.23). The transition between the $k-\varepsilon$ and the $k-\omega$ model is managed by adjusting the coefficients in the k and ω transport equations using a blending function.

$$\frac{\partial \omega}{\partial t} + \frac{\partial}{\partial x_j}(\langle v_j \rangle \omega) = P_\omega + \frac{\partial}{\partial x_j}\left[\left(\nu + \sigma_\omega \nu_t\right)\frac{\partial \omega}{\partial x_j}\right] - \beta\omega^2 \tag{2.22}$$

$$\frac{\partial k}{\partial t} + \frac{\partial}{x_j}(\langle v_j \rangle k) = P_k + \frac{\partial}{\partial x_j}\left[\left(\nu + \frac{\nu_t}{\sigma_k}\right)\frac{\partial k}{\partial x_j}\right] - \beta^* k\omega \tag{2.23}$$

The SST $k-\omega$ model also implements a limitation on the turbulent viscosity in order to reduce overestimation of shear stress. This is done by relating the turbulent time scale to both the strain rate tensor and the wall distance.

2.2.2.4 Reynolds stress model

The Reynolds Stress model (RSM) is able to account for anisotropy in the turbulence since all components of the Reynolds stress tensor are solved through their respective transport equations, as shown in equation (2.24).

$$\frac{\partial \langle v_i' v_j' \rangle}{\partial t} + \frac{\partial}{\partial x_k}(v_k \langle v_i' v_j' \rangle) = D_{ij} + P_{ij} + \Pi_{ij} - \varepsilon_{ij} \tag{2.24}$$

$$D_{ij} = \frac{\partial}{\partial x_k}\left[\left(\nu + \frac{\nu_t}{\sigma_k}\right)\frac{\partial \langle v_i' v_j' \rangle}{x_k}\right] \tag{2.25}$$

$$P_{ij} = -\langle v_i' v_k' \rangle \frac{\partial v_j}{\partial x_k} - \langle v_j' v_k' \rangle \frac{\partial v_i}{\partial x_k} \tag{2.26}$$

The turbulent kinetic energy is calculated directly from the Reynolds stresses as half the sum of the normal stresses in the Reynolds stress tensor, $\frac{1}{2}R_{ii}$. The turbulent viscosity can then be obtained as following:

$$\nu_t = c_\mu \frac{k^2}{\varepsilon}. \tag{2.27}$$

The most recent and accurate version of RSM implemented in Simcenter STAR-CCM+ is the Elliptic Blending model. This model is capable of handling both low and high y^+ [15], where y^+ is the dimensionless wall distance. The Elliptic Blending model acts on the pressure strain term Π and dissipation ε in the RSM transport equations through the elliptic blending coefficient α_{EB}. The blending coefficient allows for formulations in near-wall regions and homogeneous flow regions, as described in equation (2.28).

$$\Pi_{ij} - \varepsilon_{ij} = (1 - \alpha_{EB}^3)(\Pi_{ij}^w - \varepsilon_{ij}^w) + \alpha_{EB}^3(\Pi_{ij}^h - \varepsilon_{ij}^h) \tag{2.28}$$

The elliptic blending technique allows for usage of the near-wall formulation for the quadratic pressure strain term in regions close to walls, while transitioning to the linear pressure strain formulation in the homogeneous flow. The formulation of the dissipation varies by assuming isotropic dissipation in the homogeneous flow, while relating it to the Reynolds stresses near the walls.

2.2.3 Large eddy simulation

Large eddy simulation (LES) is a model to solve large scale turbulence. In contrast to RANS, instantaneous equations are solved to capture temporal fluctuations. The computational mesh however acts as a filter that determines the scale of spatial fluctuations that are solved and all properties solved are a spatial average over the cell. Similar to temporal averaging, one property can be decomposed into a spatial average and a spatial fluctuation

$$\Phi = \bar{\Phi} + \Phi'' \tag{2.29}$$

where the spatial average in one direction, in this case x with Δx being the cell length, is defined as

$$\bar{\Phi}(x,t) = \frac{1}{\Delta x}\int_{x-0.5\Delta x}^{x+0.5\Delta x} \Phi(\xi,t)\, d\xi. \tag{2.30}$$

The Navier-Stokes equations for incompressible flow with the spatial filtered variables becomes

$$\frac{\partial \bar{v}_i}{\partial x_i} = 0 \tag{2.31}$$

$$\frac{\partial \bar{v}_i}{\partial t} + \frac{\partial}{\partial x_j}(\bar{v}_i\bar{v}_j) = -\frac{1}{\rho}\frac{\partial \bar{p}}{\partial x_i} + \nu\frac{\partial^2 \bar{v}_i}{\partial x_i \partial x_j} - \frac{\partial \tau_{ij}}{\partial x_j} \tag{2.32}$$

where τ_{ij} represents the subgrid stresses [14]. The subgrid stresses needs to be modeled and is most commonly done so with the Smagorinsky model as

$$\tau_{ij} - \frac{1}{3}\delta_{ij}\tau_{kk} = -2\nu_{sgs}\bar{s}_{ij} \tag{2.33}$$

where the subgrid viscosity is calculated as

$$\nu_{sgs} = (C_S(\Delta V)^{1/3})^2|\bar{s}|. \tag{2.34}$$

2.2.3.1 Spatial descritization

LES is always mesh dependent since the mesh acts as a spatial filter, deciding what scales of turbulence are resolved and what scales are modeled. There exist several methods to evaluate what scales have been resolved in order to evaluate the LES, that requires a solution to base the evaluation on. In order to minimize the resources it is therefore beneficial to find a sufficiently fine mesh through evaluation prior to the simulation. Such an evaluation is done by comparing the mesh to the turbulent length scales obtained from a RANS simulation. The upper limit of the inertial sub-range in the energy spectra is the integral length scale l_0, and can be calculated from RANS results as in equation (2.35). In order to resolve the largest eddies the

mesh cell size must be several times smaller than l_0. The exact number of cells needed per integral length scale is however not clear, introducing an uncertainty when defining the mesh.

$$l_0 = \frac{k^{3/2}}{\varepsilon} \tag{2.35}$$

The lower side of the inertial sub-range in the energy spectra is represented y the Taylor micro scale λ, which can be calculated with equation 2.36. In turbulent channel flow, it has been showed to be successful to set the cell size equal to λ in order to resolve large eddies in LES [17].

$$\lambda = \sqrt{10\nu\frac{k}{\varepsilon}} \tag{2.36}$$

The draw back of LES is however that the size of the large turbulent scales becomes very small near walls, thereby increasing the requirements on mesh resolution.

2.2.4 Detached eddy simulation

The Detached Eddy Simulation (DES) combines LES and RANS by utilizing their respective strengths. In DES, LES is used in the free stream region to resolve large scale turbulence, while small scales are modeled with a subgrid model. On the other hand, RANS works well within boundary layers and is therefore used near walls to model all turbulence, thereby reducing the computational demand compared to using LES in the whole domain.

The transition from RANS to LES is handled by modifying the dissipation term in the transport equation of k so that the dissipation increases when the LES is active. This is achieved by multiplying the dissipation term with a blending function, which typically considers factors such as cell size, turbulent length scale, and wall distance.

2.2.5 Wall functions

The interaction between the fluid and walls give rise to a boundary layer near the wall. Within the boundary layer, the fluid is largely affected by viscous forces as the velocity of the fluid transitions from the free-stream velocity to zero relative velocity at the wall. The thickness of the boundary layer is often defined as the distance from the wall where the fluid reaches 99% of the free-stream velocity. In turbulent flow, the boundary layer is divided into an outer and an inner layer. The outer layer is dominated by turbulent forces, while the inner layer is divided further into three sublayers, which are defined by the dimensionless wall distance y^+

$$y^+ = \frac{yu^*}{\nu} \tag{2.37}$$

where y is the distance to the nearest wall and u^* is the frictional velocity, which is related to the shear stress on the wall.

- **Viscous sub-layer**: The fluid closest to the wall is dominated by viscous forces and the flow is almost laminar. $y^+ < 5$.
- **Buffer layer**: Transitional layer between the viscous sub-layer and the log layer. $5 < y^+ < 30$.
- **Log layer**: The fluid is affected equally by viscous and turbulent forces. $30 < y^+$.

For simulations that do not fully resolve all the physics near walls, certain quantities such as velocity and turbulence can be approximated within the sublayers of the inner boundary layer using wall functions. These wall functions are based on empirical data and are defined for the viscous sub-layer and the log layer. Simcenter STAR CCM+ uses blended wall functions that are continuous throughout the entire inner boundary layer, which provides better accuracy in the buffer layer [15]. The blended wall function however has higher accuracy in the viscous sub-layer and log layer than the buffer layer.

2.2.6 Volume of fluid

The Volume of Fluid (VOF) method is a numerical method used to solve the interface between different phases in fluid flows. VOF uses an Eularian approach where the interface is tracked by solving the continuity equation of a indicator function of each phase. In Simcenter STAR-CCM+, the indicator function is defined as the volume fraction of each phase, denoted $\alpha_{VOF,i}$, where i represents the phase. The volume fraction is defined as the ratio of the volume of a particular phase to the total volume, as described in equation (2.38) [15].

$$\alpha_{VOF,i} = \frac{V_i}{V} \tag{2.38}$$

The transport of α_i is solved according to equation (2.39) with the constraint that the sum of volume fractions must equal unity, for two phases the transport is hence only solved for one phase.

$$\frac{\partial \alpha_i}{\partial t} + v_j \frac{\partial \alpha_i}{\partial x_j} = 0 \tag{2.39}$$

The field equations are solved by treating the mixture as a single phase with properties determined by the volume fraction, $\rho = \sum_i \alpha_i \rho_i$ and $\mu = \sum_i \alpha_i \mu_i$.

2.2.7 Passive scalar

The transport of a species in a fluid can be represented as a passive scalar, which is a scalar quantity that does not affect the flow. The transport of the passive scalar is solved through diffusion and convection based on the flow field, as shown in equation (2.40).

$$\frac{\partial \phi}{\partial t} + \frac{\partial \phi v_i}{\partial x_i} = \frac{\partial}{\partial x_i}\left[\left(\frac{\nu}{Sc} + \frac{\nu_t}{Sc_t}\right)\frac{\partial \phi}{\partial x_i}\right] \tag{2.40}$$

The diffusivity of the passive scalar depends on Schmidt number, Sc, which represents the molecular diffusivity of the scalar in the fluid, and the turbulent Schmidt

number, Sc_t, which represents an artificial diffusivity based on the modeled turbulence. The turbulent Schmidt number depends on the flow field and can vary locally, making it difficult to determine. A typical value of the turbulent Schmidt number in stirred tank configurations is $0.2 < Sc_t < 0.9$, and it is often used as a tuning constant when simulating mixing times.

2.2.8 Rotating bodies

The rotation of the impeller is represented using multizone methods, which divide the domain into two zones. One zone contains the rotating impeller and the fluid in its proximity, while the other zone contains the rest of the domain. The benefit of using a multizone method is that the mesh only needs to be generated once while adjusting the position of the impeller itself would have required a new mesh every time step. Figure 2.1 shows the different zones. The rotating region, including the impeller is shown in a yellow color.

Figure 2.1: Fluid domain divided into the different zones. The rotating region, containing the impeller in yellow and the stationary region in grey.

2.2.8.1 Multiple Reference Frame

The multiple reference frame (MRF) method represents the rotation of the impeller by solving the flow in proximity to the impeller with a reference frame rotating with the impeller. A source term is added to the cells in the region that contains the impeller to simulate the effect of rotation. The effect of the source term is propagated through the interface onto the stationary region. The impeller thus remain stationary and the mesh is fixed in position throughout the simulation. Since the mesh remains fixed the MRF results are dependent on the original position of the impeller blades. This approach makes it possible to simulate moving bodies in a steady state and thus limiting the computational cost. By using this method it is assumed that the flow around the impeller is weakly linked and located far away from other features in the tank that could disrupt the flow.

2.2.8.2 Sliding mesh

The sliding mesh (SM) method allows for a moving mesh and creates a real rotation of the impeller, unlike MRF. Each time step the mesh of the region that contains the impeller "slides" into a new position relative to the stationary region, and information is interpolated between the regions. This method offers transient results that does not depend on the initial position of the impeller blades but still without the need to create a new mesh each time step. SM is assumed to be more accurate than MRF but also more computational expensive since the simulations are required to be transient.

3 Methods

The forthcoming chapter outlines the methodology employed to prepare and conduct experiments and simulations to investigate the mixing process in the tank under four different operational conditions, as detailed in Table 3.1. The volumes and velocities were chosen such that a vortex would form in case 3 and 4 but not in case 1 and 2. The Reynolds number for all cases were well above the range where the flow in stirred tanks usually transitions to fully turbulent.

Table 3.1: Water level and impeller velocity for the four studied cases. Case 3 and 4 formed a vortex. The *Re* indicates that all cases were fully turbulent.

Case	1	2	3	4
Water level [mm]	408	408	816	816
Impeller velocity [rpm]	208	262	268	337
Reynolds number [-]	75800	95500	97600	123000

The mixing process was conducted in a tank with a diameter of 680 mm, with the ZG5 magnetic impeller from Metenova, which has a diameter of 148 mm. The impeller was mounted on an eccentrically positioned shaft within the tank, as seen in Figure 3.1. The studied impeller rotated in the negative direction around the axial axis of the impeller, with the positive axial direction upwards along the center line of the impeller.

(a) Cross section view of the tank. (b) Metenova ZG5 impeller.

Figure 3.1: View of the tank setup and the impeller which were used in experiments and simulation.

3.1 Physical experiments

The physical experiments were carried out at Metenova's test lab, where the mixing time and impeller torque were measured. The torque was measured using a sensor with an operating range of 0-30 Nm, and was mounted on the output shaft of the motor. To validate the accuracy of the torque sensor, it was compared to two torque wrenches at various points within the operating range. The torque sensor exhibited a variation of ± 0.1 Nm from the nominal value.

Saline was used as the tracer liquid, which consisted of sodium chloride (NaCl) mixed with tap water until the salt was completely dissolved. The mixture consited of 16.7 mass% NaCl. For the experiments, 100 g of tracer liquid was poured onto the water surface over a duration of approximately 3 seconds. In order to study the potential impact of the application point of the tracer on the mixing time, measurements were conducted with the tracer added at two different locations on the surface. Each application point was tested three times. Furthermore, an additional experiment was performed to investigate the effect of the amount of tracer liquid on the mixing time, where the quantity of the tracer liquid was doubled.

To assess the mixing time, conductivity in the water was measured at three distinct locations within the tank. The conductivity was directly used as a measurement of concentration since the conductivity is linearly dependent on the concentration of NaCl at concentrations below one mole per litre [18], which quickly became the case when the tracer was mixed in the tank. TetraCon 925 conductivity cells, depicted in Figure 3.2, were employed as probes. Two probes were positioned near the water surface, while one was placed close to the bottom. The diameter of the probes was approximately 15 mm, and their orientation was aligned with the flow at each respective location. The conductivity probes were initiated simultaneously with the addition of the tracer liquid, and measurements were taken every second until a steady state was achieved. The location of the conductivity probes and the application points of the tracer are illustrated in Figure 3.3.

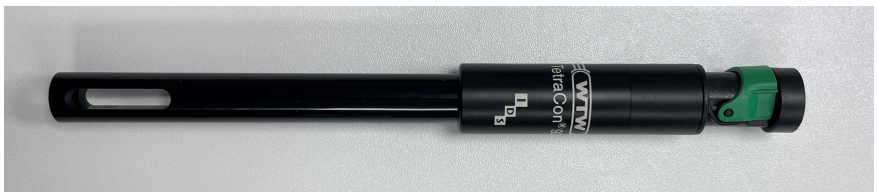

Figure 3.2: One of the probes used to measure conductivity. The hole in the probes was aligned with the flow field.

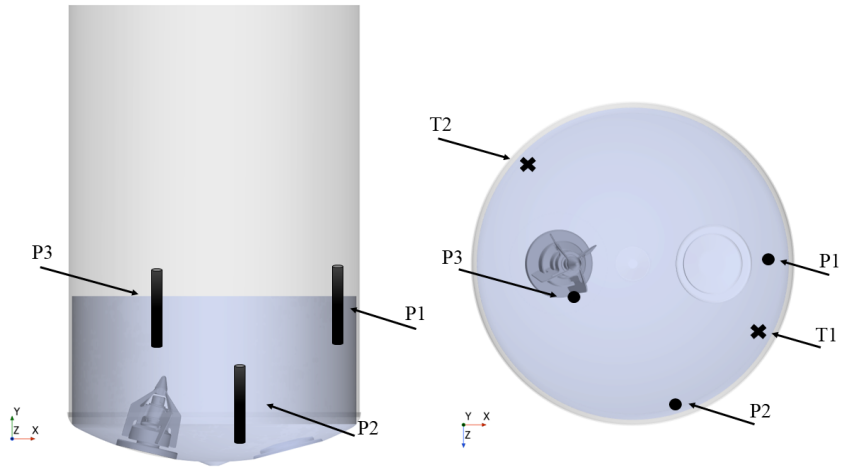

(a) Measurement and tracer location for case 1 and 2

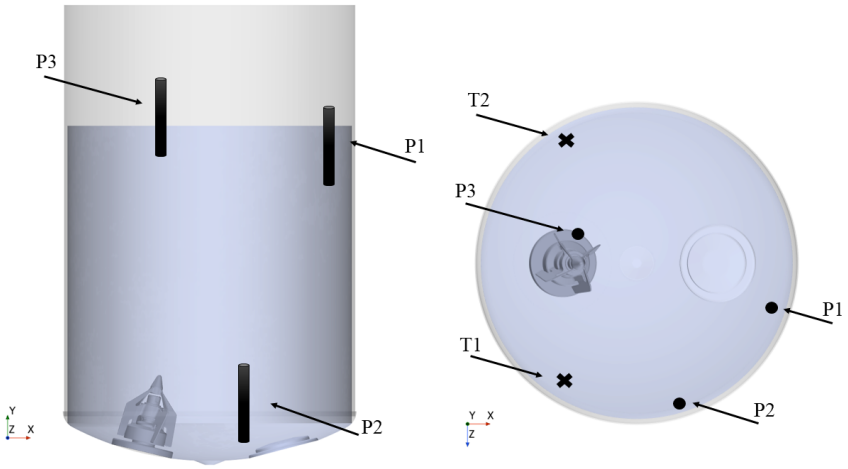

(b) Measurement and tracer location for case 3 and 4

Figure 3.3: The placement of the three conductivity probes and the two tracer application points. The probes are marked P1, P2 and P3 and the two tracer application points are marked T1 and T2.

3.2 CFD simulations

The method of setting up the CFD simulations was based on both literature and conducted studies, which are presented in this section. Steady-state and transient simulations were performed for all four cases. In the transient simulations of cases 3 and 4, where a vortex was expected, the free surface was solved using the VOF method. In all other simulations, the top surface was fixed and modeled as a free slip wall. The impeller and tank walls were modeled with a no-slip condition.

3.2.1 Rotational motion

In the transient simulations, the SM method was employed to capture possible transient effects from the impeller. When using the SM method, a guideline is to select a time step such that the impeller rotates by 1° in each time step [15]. Another criterion was to ensure that the mesh movement on the interface between each time step is smaller than the length of the cells on the interface. Among the criteria considered, the 1° rotation proved to be the most conservative and thus determined the time step used in the simulations, resulting in time steps ranging from $0.0005 - 0.001$ s. The MRF method was utilized in all simulation studies in the methodology chapter, as well as in all steady-state simulations of the investigated cases.

3.2.2 Turbulence model

Through previous work, it has been shown that the turbulence model has a significant impact on the velocity field, which affects the pumping number, power number, and mixing time. Since the velocity field could not be captured in experiments, the choice of the turbulence model was instead based on comparisons with results obtained with DES, which has been shown to be more accurate than results obtained with RANS models. The study of turbulence models was conducted with a water level of 816 mm and an impeller speed of 337 rpm, as this case was expected to have the most swirl and thus where the anisotropy of turbulence is most pronounced.

Before conducting the mesh convergence study, an analysis of the turbulence models was performed since the choice of turbulence model could potentially influence the needed mesh size. Previous research on mixing tanks, specifically those utilizing RANS models, have typically employed meshes with approximately one million cells. For previous studies involving the same impeller as in this thesis, it was determined that a mesh with 1.3 million cells was adequately refined when using the realizable $k - \varepsilon$ model. Therefore, the comparison of turbulence models in this thesis was conducted using a mesh consisting of 1.5 million cells, with cell sizes of 10mm in the bulk flow region and 1mm on the impeller. Prism layers were implemented on the walls to maintain a y^+ value of 5 or lower.

The mesh employed for the DES simulations was determined based on the Taylor length scales obtained from RANS simulations. These length scales indicated that a cell size of approximately 4mm was adequate in the bulk flow region. As a result, a mesh with 7.9 million cells was generated. The time step used in the simulations was set to 0.002 seconds, yielding a maximum CFL number of approximately 5 near the impeller and below 1 throughout most of the domain. A total of 20 inner iterations were performed, leading to a decrease in residuals by three orders of magnitude within each time step.

The velocity fields obtained from different turbulence models were compared both qualitatively and quantitatively. Figure 3.4 illustrates the velocities at a plane centered in the tank. The time-averaged velocity field obtained from DES, shown in

Figure 3.4d, exhibits a thin region of low velocity starting from the top of the impeller and forming an arc towards the water surface. Around this line, there is an area of higher velocity. The velocity field obtained from RSM, Figure 3.4c, shows a similar pattern to DES. On the other hand, the velocity fields obtained from the $k-\varepsilon$ and SST $k-\omega$ turbulence models result in smoother velocity fields where the swirl is spread out and less distinct.

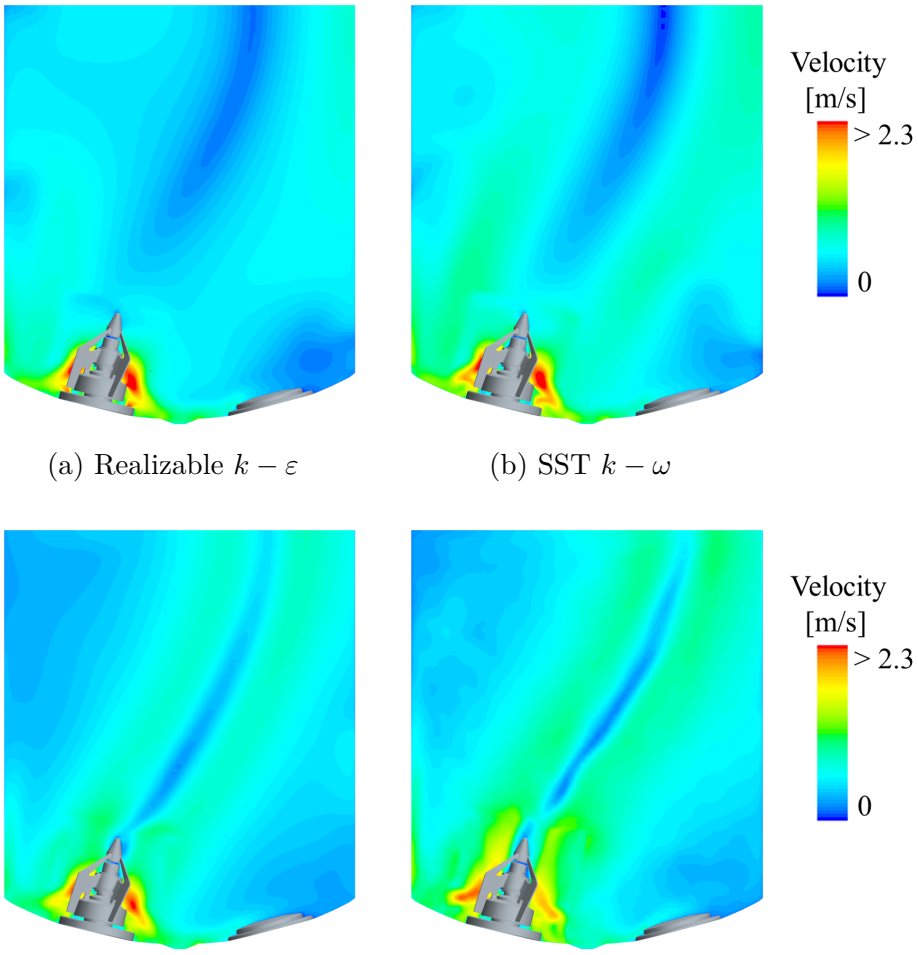

(a) Realizable $k-\varepsilon$ (b) SST $k-\omega$

(c) RSM (d) Time averaged DES

Figure 3.4: Comparison of the velocity fields between RANS models and time averaged DES at a plane in the center of the tank.

In Figure 3.5, the velocities along the centerline of the tank are compared for different turbulence models. The RSM and DES results exhibit clear swirling patterns, although the location of the swirl differs between the two models. DES generates higher velocities around the swirl compared to RSM. Overall, RSM was considered to be the most accurate RANS model for this application, while the velocity field with $k-\varepsilon$ differed the most from DES. Based on these findings, both RSM and SST $k-\omega$ models were used for further analysis, considering the significant computational demands of RSM.

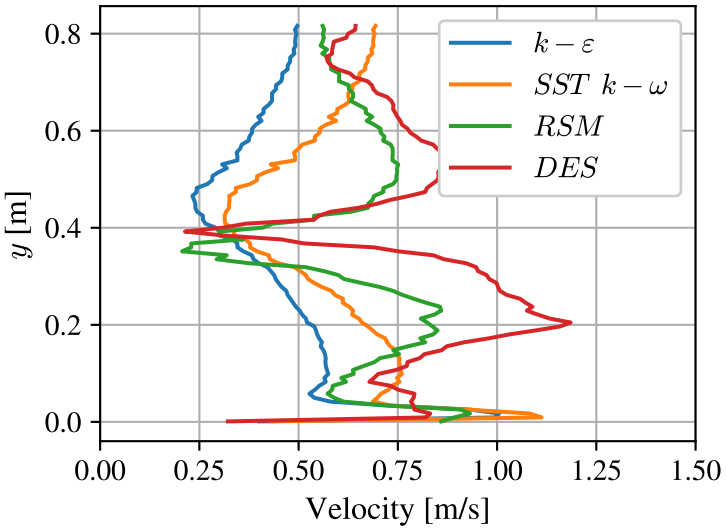

Figure 3.5: Comparison of velocity magnitude on the centerline of the tank ($x = 0$, $z = 0$) between RANS models and time averaged DES.

3.2.3 Mesh

The polyhedral mesh type was chosen to generate a volume mesh together with prism layers to accurately capture the flow characteristics near the walls. A mesh independence study was performed to select a mesh resolution that generated converged results without adding unnecessary computational cost. The power number, mixing time and velocity magnitude were monitored and compared for different mesh settings in order to determine the final mesh.

The impeller serves as the primary source of turbulent flow, leading to high gradients of the time-averaged variables in its vicinity. Therefore, a fine mesh was necessary near the impeller to capture these gradients accurately. To determine the size of these cells, a surface target size was defined on the impeller surface. The size of the cells in the bulk flow in the tank were determined by the maximum cell size. It was desirable to have the same cell size on both sides of the rotating interface, cells on the interface were kept as 50% of the maximum cell size.

In order to address convergence issues it was desirable to keep y^+ below 5 on the tank walls. y^+ on the impeller walls was lower, ~ 1, to keep the outer prism layer smaller than the core mesh. The prism layers on the tank walls had six layers and the impeller walls had seven layers.

3.2.3.1 Mesh convergence study

The RSM model was employed for the mesh independence study, as it is generally more challenging to converge compared to the $k-\omega$ model. The rotation was modeled using the MRF approach, with a rotational speed of 337 rpm. The water height was set at 816 mm, and a slip-wall boundary condition was applied to the top

surface. The MRF approach was chosen to enable steady-state simulations, which significantly reduced computational cost. Six different meshes were utilized in the study, with variations in the maximum cell size and impeller cell size. The prism layers remained constant across all cases. Table 3.2 provides information on the maximum cell size and target surface sizes for each of the six meshes.

Table 3.2: Settings for mesh independence study of the core mesh with the RSM model

Control	M1	M2	M3	M4	M5	M6
Maximum cell size [mm]	30	15	15	10	8	6
Target surface size on impeller [mm]	2	1.2	1	0.9	0.8	0.8
Number of cells [million]	0.46	0.75	1.27	1.74	2.40	3.40

The different meshes are evaluated based the averaged velocity, power number and the mixing time where the tracer fluid is represented as a passive scalar. The results are shown in Figure 3.6 and it can be seen that the variation between the meshes decreases with increased resolution.

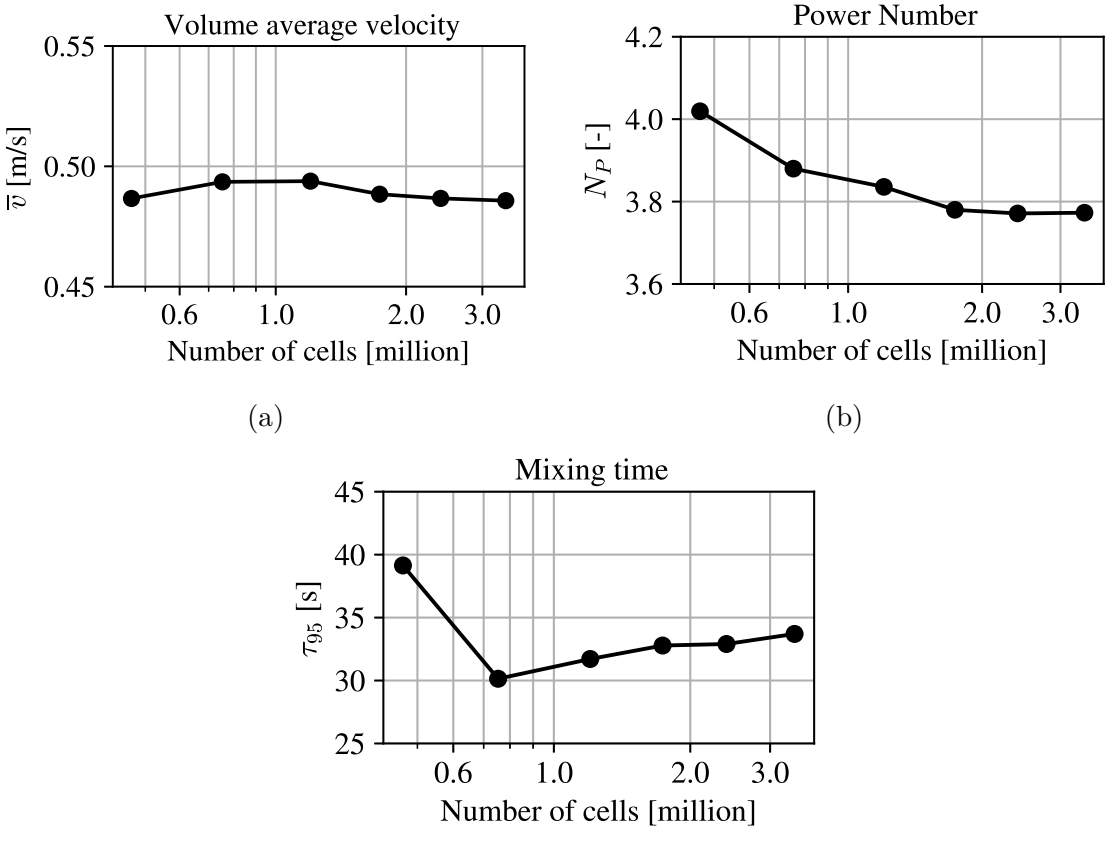

Figure 3.6: Core mesh convergence study of case 4 using the RSM model. Three parameters were monitored, volume average velocity (a), power number (b) and mixing time (c).

The meshes were also compared in Figure 3.7 based on the velocity magnitude along the center line of the tank, where it can be seen that the meshes $M4$, $M5$ and $M6$ resulted in a similar velocity profile.

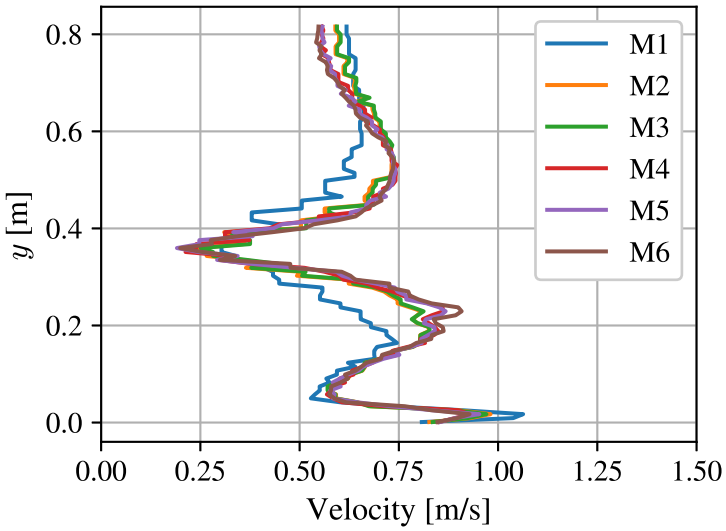

Figure 3.7: Velocity magnitude along the center line of the tank ($x = 0$, $z = 0$) for six different meshes where $M1$ is the coarsest and $M6$ the finest. y is the distance from the bottom of the tank.

The mesh labeled as *M4* forms a knee point in Figure 3.6b, indicating that the difference relative to the mesh size decreases significantly. Therefore, *M4* was chosen for the subsequent simulations, and its structure is seen in Figure 3.8.

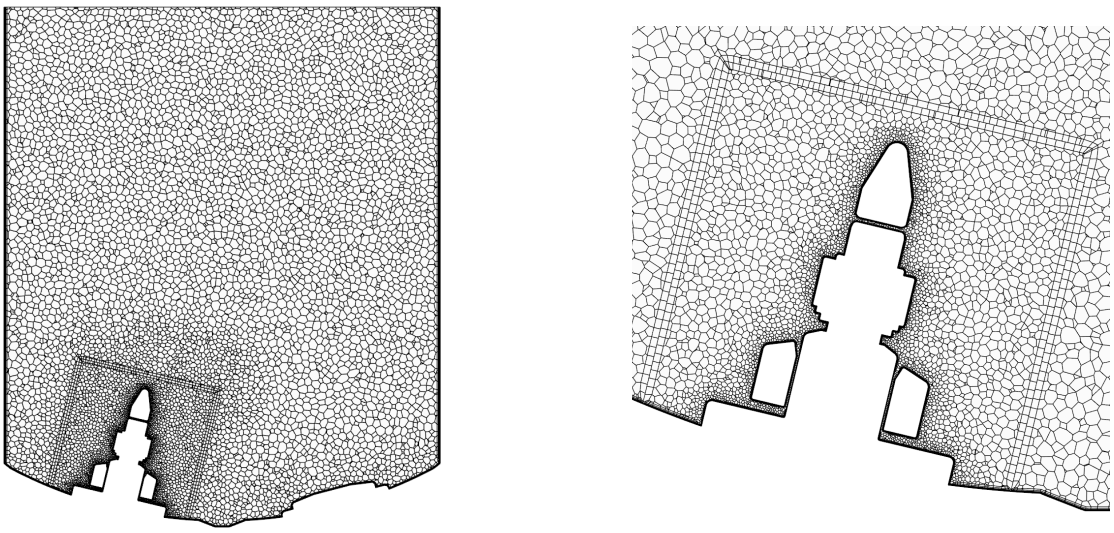

(a) Volume mesh in the XY-plane

(b) Mesh in the rotational volume surrounding the impeller

Figure 3.8: Cross sectional views of mesh $M4$ that is chosen as the base mesh in simulations of all cases.

In Figure 3.8b the interface between the stationary and rotating region can be seen around the impeller. The size of the rotating region was chosen to minimize gradients of field variables over the interface while being subjected to the constrain that the interface must be axisymmetric. One prism layer was used on each side of the interface based on the recommendation in the documentation for Simcenter STAR-CCM+ [15] to enhance stability in the simulation.

3.2.3.2 Mesh refinement around free surface

The mesh $M4$ was refined in regions where the interface between water and air was present in simulations using the VOF method. The first refined mesh, $R1$, was generated by reducing the cell size to 5 mm around the water surface and the vicinity of the expected vortex. A second refined mesh, $R2$, was made by reducing the cell size around the water surface to 4 mm and in the vicinity of the expected vortex to 2 mm. The two refined meshes are shown in Figure 3.9 and were compared through simulation with VOF of case 4.

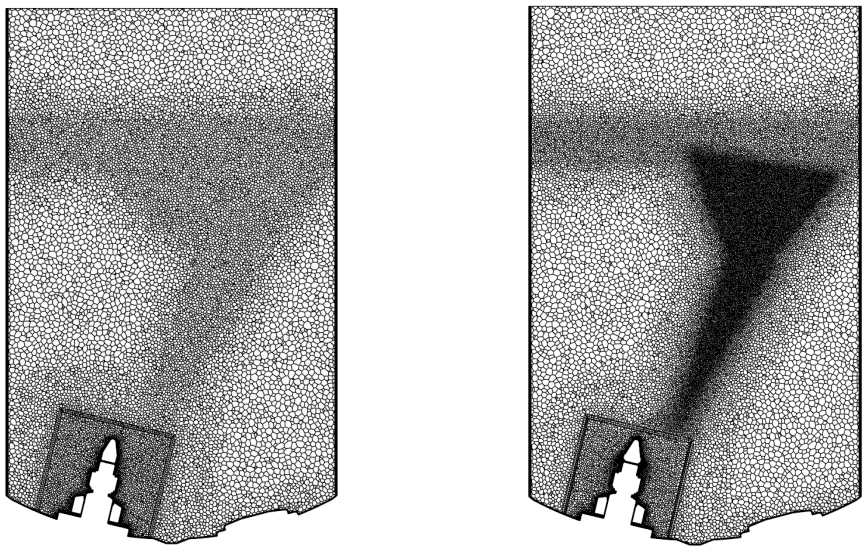

(a) Mesh $R1$. Cell size of 5 mm in the refined area.

(b) Mesh $R2$. Cell size of 2-4 mm in the refined area.

Figure 3.9: Cross sectional view in the XY-plane of mesh $R1$ and $R2$. The mesh in 3.9b was used in transient simulations of cases 3 and 4.

VOF simulations of case 4 with the $R1$ and $R2$ meshes in Figure 3.9 resulted in similar impeller parameters, with a difference of ~ 3 % between the meshes. The vortex captured by tracking the free surface increased in size and was less prone to breaking up with increased mesh resolution. Further more, the mass conservation error of the water phase decreased with over 50 % in with mesh $R2$ compared to $R1$. With the mesh $R2$, the accumulated mass conservation error was 10 g after 11 s, which is equivalent to 0.004 % of the total mass of the water phase. Based on this results, the mesh $R2$ in Figure 3.9b was chosen for further simulations. The

mesh was however not refined further due to the small difference of the impeller parameters.

3.2.4 Pumping number

The volumetric flow rate required to calculate the pumping number was obtained by integrating the velocity of the outflow over a cylindrical surface swept around the impeller [12]. The diameter of the cylinder was chosen to be 150 mm, which is 2 mm larger than the impeller diameter. The cylinder extends from the plate on which the impeller is mounted and upwards, shown in Figure 3.10.

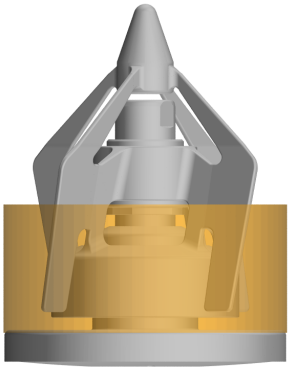

Figure 3.10: The orange cylinder around the impeller shows the swept area on which the flow rate was calculated by integrating normal velocities. The bottom of the cylinder was fixed while the height was set to result in the maximum flow rate. The diameter of the cylinder is 150 mm which is 2 mm larger than the widest point of the impeller.

The height of the cylinder was selected to capture the maximum outflow, taking into consideration the avoidance of water passing in to the cylinder sides at the top, which would result in a lower flow rate. In all simulations, the volumetric flow rate was monitored for six different heights of the swept cylinder, and the pumping number was calculated based on the highest obtained value. Figure 3.11 illustrates an example of how the pumping number varied for cylinder heights ranging from 40 mm to 70 mm. In this particular case, the established pumping number was 0.65.

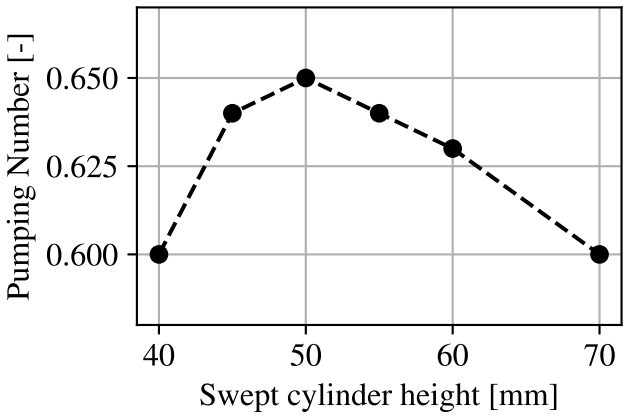

Figure 3.11: Plot showing how the pumping number varied for different heights of the swept cylinder.

3.2.5 Free surface modeling

The free surface was treated using the Volume of Fluid (VOF) method in the transient simulations of cases 3 and 4. In these simulations, the surface tension force was not included in the model. This decision was based on the high Reynolds number, where the inertial forces in the fluid were expected to be much larger than the surface tension forces. The CFL number at the interface was below unity due to the size of the time step that was limited by the rotational speed of the impeller.

3.2.6 Mixing time

In the simulations, the tracer fluid was modeled as a passive scalar, neglecting its impact on the flow field. This choice was motivated by the similarity between water and saline properties, and previous studies with the same geometry have shown that the difference in viscosity has a negligible effect on the results [7]. The Schmidt number, which was also found to have a negligible effect on the mixing time, was set to 450 based on the self-diffusion of water with a molecular diffusion of $2.3 \cdot 10^{-9}$ m^2/s. The turbulent Schmidt number was set to 0.7.

To reduce the computational cost, the transport of the passive scalar was solved on frozen flow fields obtained from both steady and transient simulations for all cases. The transient simulations were run until a quasi-steady state was reached. In cases 3 and 4, which involved the presence of a vortex, the water-air interface was solved using the volume of fluid (VOF) method. Once the vortex had stabilized, it was treated as a wall with slip conditions. The velocity field was then solved after placing the slip wall on the free surface, and the solution was allowed to stabilize, which took approximately half a second. This approach ensured that the tracer remained within the water phase by enforcing zero normal velocities on the free surface.

The passive scalar was initialized in a volume of 100 cm^3 just below the water

surface at the second tracer location (T2), where the saline was added during the experiment. The mixing time was measured using both point measurements, to compare with the probes from the experiments, and the coefficient of variation (CV) based on all cells.

4 Results

The results are presented for both experiments and the different simulation methods in order to enable comparison. The analysis of results is focused towards cases with a vortex, in alignment with the purpose and objective of this thesis.

4.1 Capturing of vortex

The basis of the CFD analysis is the resulting fields of velocities, pressure and volume fraction of water, on which the mixing metrics are later based. Significant differences in the solutions are observed in CFD simulations depending on the turbulence model employed. Therefore, results obtained with the $k-\omega$ and RSM models are presented for the operating condition with a water level of 816 mm and an impeller speed of 337 rpm.Figure 4.1 provides a comparison of the free interface between the simulations using the $k-\omega$ and RSM models. In the RSM simulation, the velocity field is initialized based on a steady solver where the water surface is defined as a slip wall. The simulation with the $k-\omega$ model is initiated from the RSM solution.

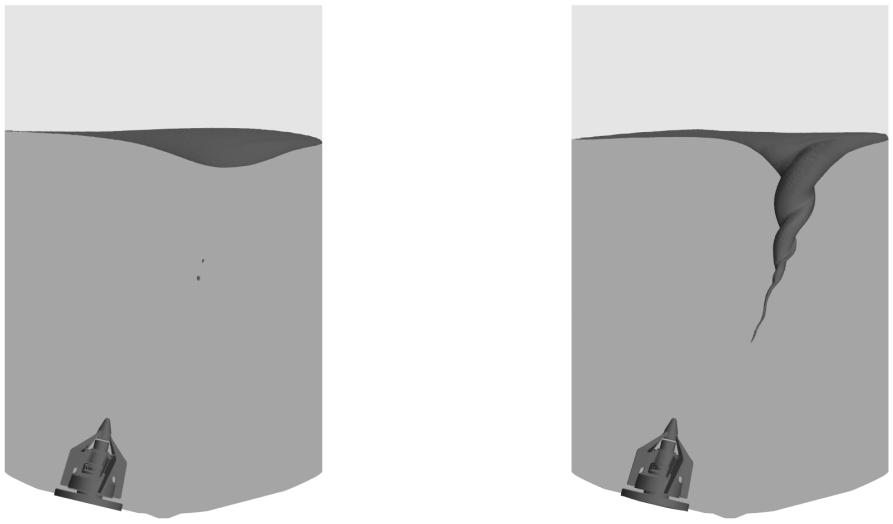

(a) SST $k-\omega$ (b) RSM

Figure 4.1: Comparison of the free surface in case 4 after reaching a quasi-steady-state with different turbulence models. The same mesh (seen in Figure 3.9b) was used in both simulations.

The SST $k-\omega$ model is unable to generate a vortex, despite starting from a solution where a vortex is present. The small air bubbles observed in the SST $k-\omega$ simulation likely result from the breakup of the vortex that was initially present. The main difference between the SST $k-\omega$ and RSM models is the assumption of isotropy in turbulence. The turbulence is studied using the resolved Reynolds stresses from the RSM simulation. The normal stresses are compared in Figure 4.2, and should be identical if the turbulence is fully isotropic..

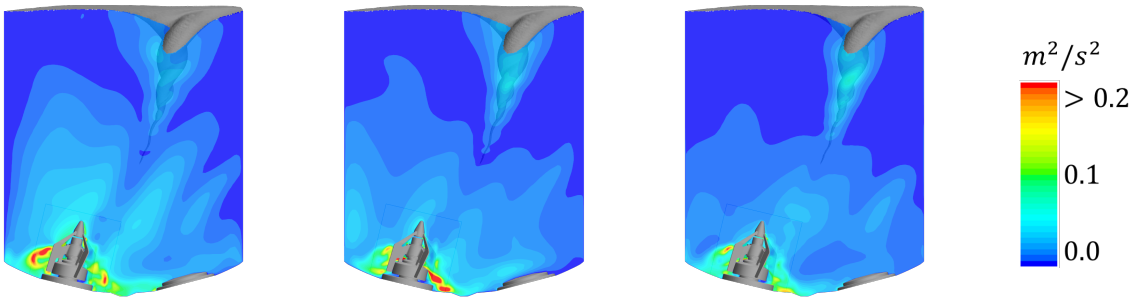

(a) $\langle \overline{v_1' v_1'} \rangle$ (b) $\langle \overline{v_2' v_2'} \rangle$ (c) $\langle \overline{v_3' v_3'} \rangle$

Figure 4.2: Normal components of Reynolds stress tensor in the XY-plane through the center of the tank. Obtained from simulation of case 4 with RSM.

The Reynolds stresses appear to be similar close to the vortex which indicates isotropic turbulence while the overall fields are clearly not identical. The degree of anisotropy is quantified by η in Figure 4.3.

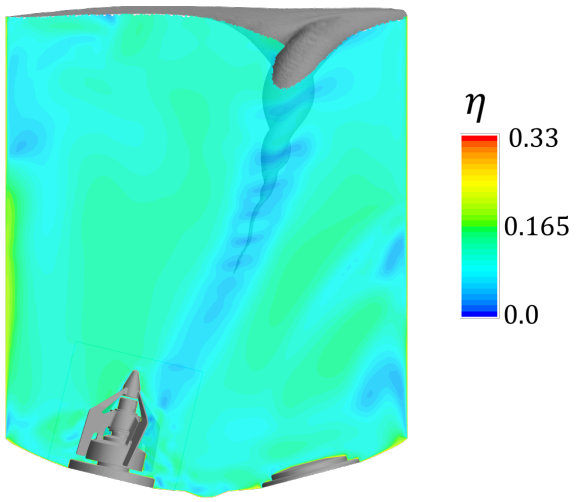

Figure 4.3: Degree of anisotropy from simulation of case 4 with RSM. The plot indicates that the turbulence is not fully isotropic in the bulk flow. A value close to zero indicate isotropic turbulence and one third correspond to one dimensional turbulence.

The highest degree of anisotropy occurs at the walls, as could be expected. However, Figure 4.3 also shows that a large part of the flow around the vortex is anisotropic,

and only a small part of the total water volume is close to being fully isotropic.

The effectiveness of using RSM is evident and is compared to the experimental results in Figure 4.4 for case 4. The simulated vortex is rendered in an attempt to generate similar distortion to the tank wall as in the experiment.

(a) Simulated vortex (b) Vortex from the experiments

Figure 4.4: Comparison of the vortex in case 4 shows that the placement and shape of the vortex is predicted well in the simulation compared to the experiment while the size is underestimated. The air bubbles between the vortex and impeller in the experiments are not resolved in the simulation.

The shape and placement of the vortex show good agreement between the simulation and experiment, with both exhibiting a screw-like shape. However, there are some notable differences. The simulation slightly underestimates the size of the vortex, and the small "string" connecting the vortex to the impeller in the experiment consists of small bubbles that are absent in the simulation. Additionally, the size of the vortex in the experiment fluctuates, while the simulation shows a stable vortex with minor fluctuations at the vortex tip. The disparity between the experiment and simulation is more pronounced in case 3, as shown in Figure 4.5.

(a) Simulated vortex (b) Vortex from the experiments

Figure 4.5: Comparison of the vortex in case 3 shows that the placement and shape at the top of the vortex is predicted well in the simulation compared to the experiment while the size is underestimated and the vortex is cut short in the simulation.

The simulated vortex closely resembles the experimental observations at the top near the horizontal water surface, both in terms of its location and shape. However, in contrast to the experimental findings shown in Figure 4.4 for case 4, the simulated vortex diminishes without thinning significantly towards the end. As a result, the size of the vortex is underestimated.

4.2 Flow field

Due to the inability of the SST $k - \omega$ turbulence model to generate a vortex, the velocity fields obtained from the Reynolds Stress Model (RSM) are deemed more accurate and, therefore, used for the remaining analysis. This assumption is further supported by the comparison of turbulence models in Chapter 3.2.2, where the RSM exhibits the closest resemblance to DES. Figure 4.6 displays the velocity fields obtained from steady and transient simulations using RSM for case 4. The streamlines demonstrate that the circulation is noticeable and similar in both simulations, but with the transient approach, the fluid near the vortex is drawn downward toward the impeller. Additionally, the velocity magnitude is generally higher in the transient case, particularly in the vicinity of the vortex.

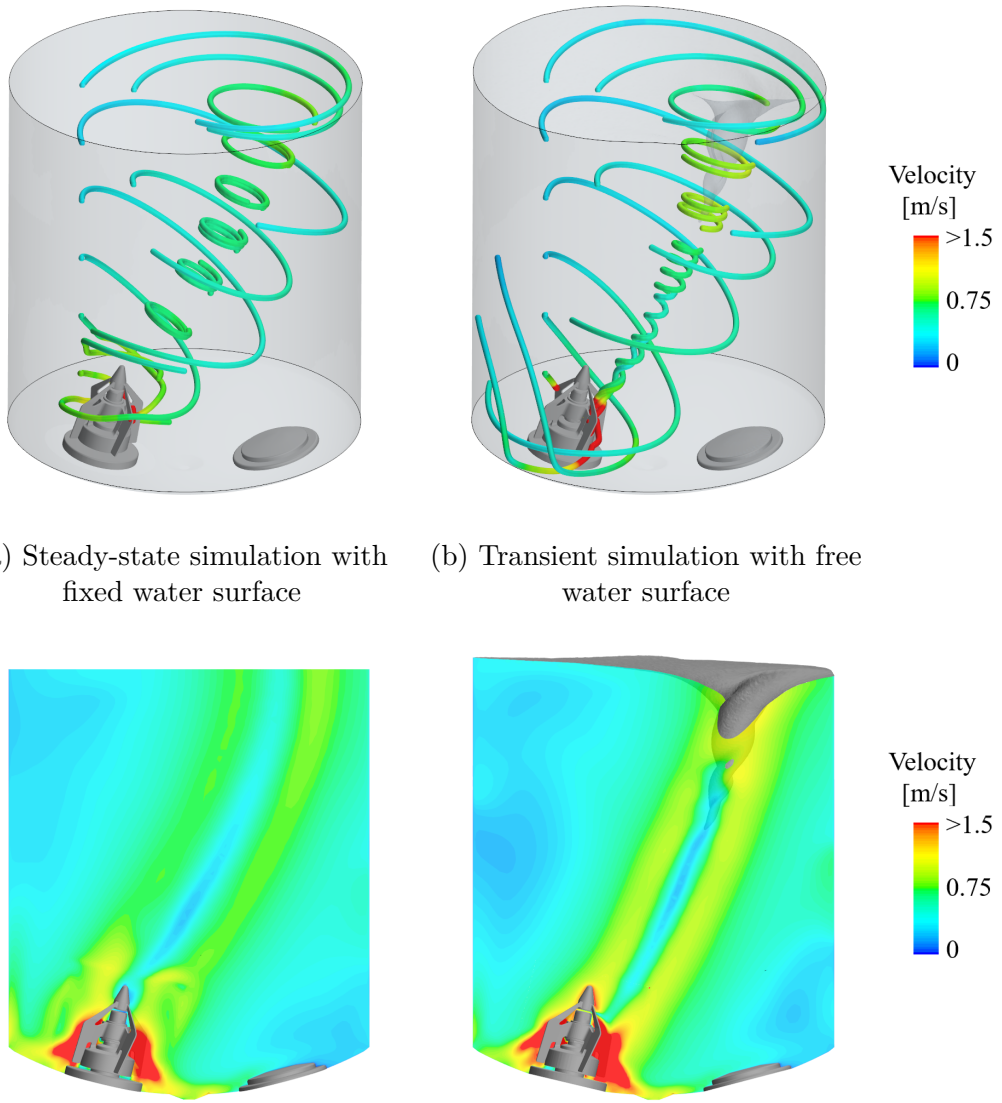

(a) Steady-state simulation with fixed water surface

(b) Transient simulation with free water surface

(c) Steady-state simulation with fixed water surface

(d) Transient simulation with free water surface

Figure 4.6: Comparison of the velocity field from steady-state simulation with a fixed water surface and transient simulation with a free water surface of case 4. The streamlines shows circulation of the fluid in both simulations but the fluid is also dragged down towards the impeller in the transient simulation.

4.3 Impeller constants

The power number is determined through torque measurements in both the experiments and simulations, utilizing equation (2.2), and is depicted in Figure 4.7. During the experiments, fluctuations in the impeller torque led to corresponding variations in the power number. Hence, the minimum, maximum, and average values obtained over a 10-second interval are reported, with the error bars representing the range. The simulations employed two approaches. Firstly, a steady case was simulated, fea-

turing a fixed water surface and rotation modeled using MRF. Secondly, a transient case was simulated using the sliding mesh (SM) method, coupled with the volume of fluid (VOF) method to solve the free surface in cases 3 and 4, where a vortex is present. In cases 1 and 2, where no vortex exists, the water surface remains fixed in both the steady and transient simulations.

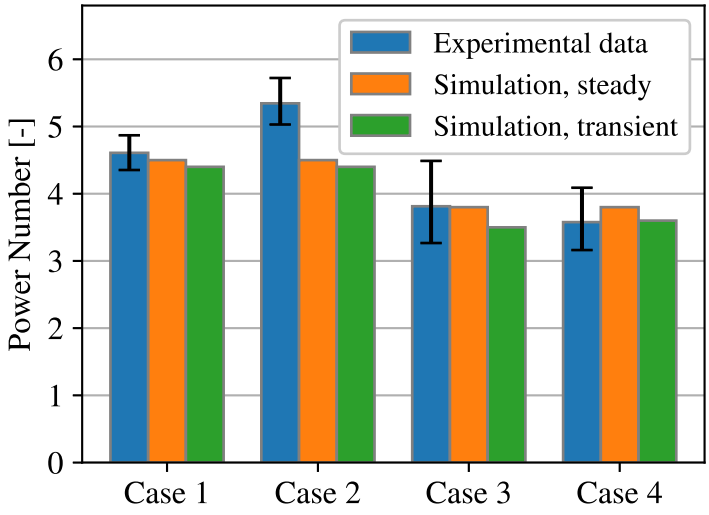

Figure 4.7: Power number obtained from experiment and simulations of the cases defined in Table 3.1. The error bars for the test data shows minimum and maximum values obtained. The power number decreases when the water volume is larger and a vortex is present (case 3 and 4).

The power number is almost constant over different impeller speeds where the water volume is the same. The power number is expected to be constant for impeller speeds with the same water volume since all conditions are fully turbulent and the obvious outlier is the experimental results from case 2.

The pumping number is obtained by measuring the volumetric flow rate through the impeller as explained in Chapter 3.2.4 and using equation (2.4). The pumping number is obtained with steady and transient simulations, similar to the power number, and is presented in Figure 4.8.

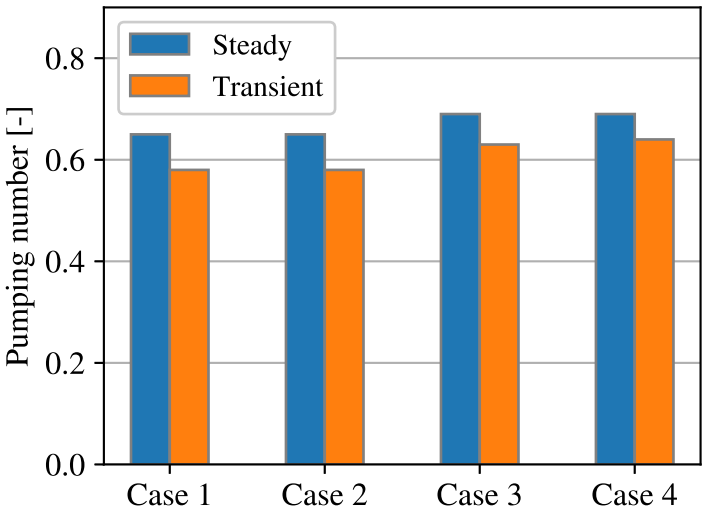

Figure 4.8: Pumping number obtained from steady and transient simulations the cases defined in Table 3.1. The pumping number is Reynolds number independent and also show to be affected to a low degree by the water level.

The pumping number is constant for different rotational speeds with the same water volume. The pumping number is also similar between large changes in water level and the presence of a vortex or not. The difference between steady and transient simulations is consistently around 5% for all cases.

4.4 Mixing

The mixing of the tracer fluid is compared through the mixing times obtained from experiments and simulations. The results from the impeller constants are then used to check the correlation with the mixing time.

4.4.1 Experimental mixing

The mixing time based on probe measurements is taken as the time it takes for all probes to be within the tolerance. An example of one experimental measurement can be seen in Figure 4.9 where the third measurement is shown for case 4 when the tracer was added at the second position. No significant variations in mixing time were observed regarding different tracer application points or volumes of tracer liquid.

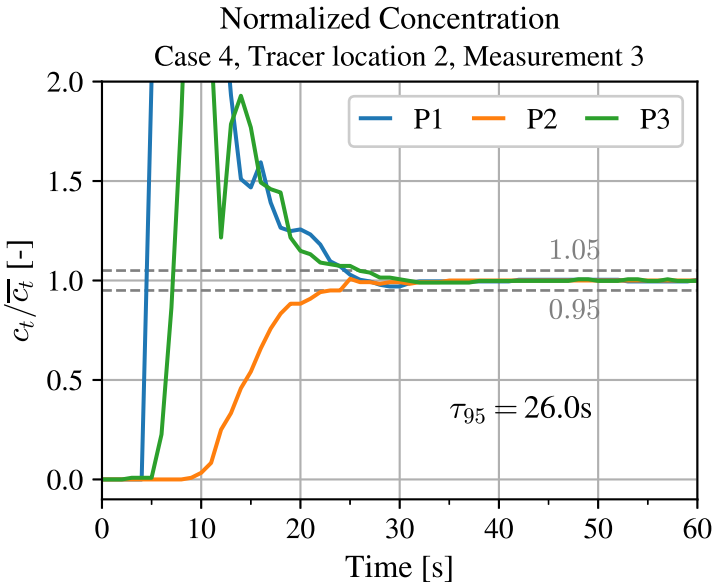

Figure 4.9: Example of normalized probe readings from the third measurement at the second aplication point of the tracer for case 4. The measured mixing time is 26.0 s. Probe 2, P2, is placed at the bottom of the tank while the other two are placed at the top.

The mixing time of the measurement in Figure 4.9 is 26 seconds which is the point when the normalized concentration of the tracer fluid is within the limit at all probes. The experimental mixing time for each case is taken as the average mixing time for all six measurements of each case (three measurements at two tracer locations) since the application point of the tracer is found to affect the transient response from the probes but not the mixing time. The results for each case are seen together with the simulation results in Figure 4.13 and all conductivity measurements are found in Appendix A.

4.4.2 Simulation of mixing

The simulation of the mixing is done by introducing a passive scalar in the second location where the tracer was added in the experiments. The mixing is studied on fields obtained with both a steady-state approach and as a transient case. The spread of the passive scalar for case 4 over time can be seen in Figure 4.10 and 4.11. Similar plots for the other cases can be found in Appendix B.

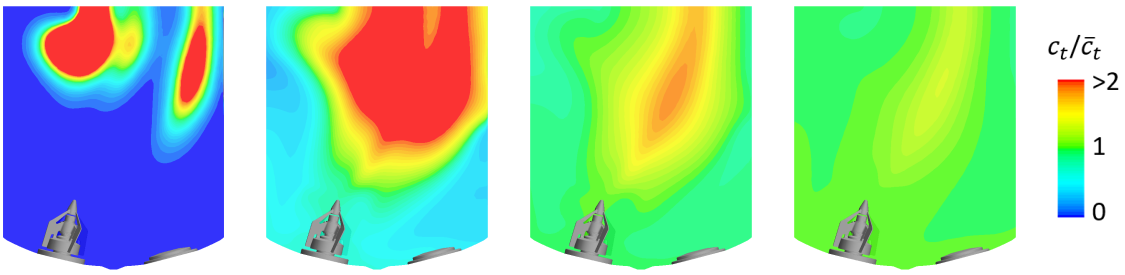

(a) 2 s (b) 10 s (c) 18 s (d) 25 s

Figure 4.10: Normalized tracer concentration at different times for case 4, the passive scalar was applied in a flow field obtained from a steady simulation with fixed water surface.

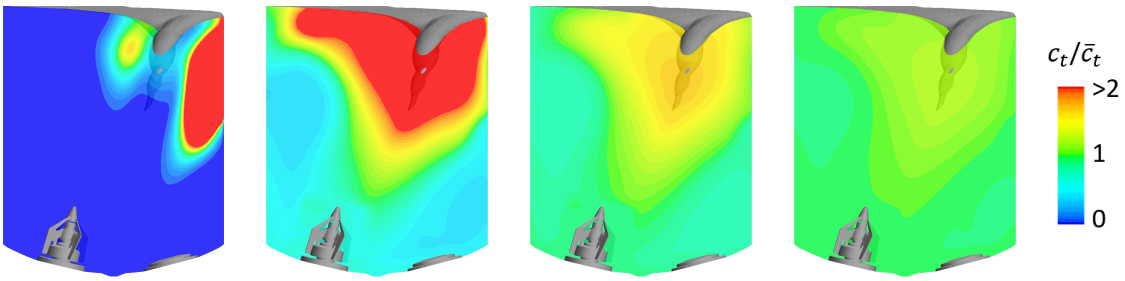

(a) 2 s (b) 10 s (c) 18 s (d) 25 s

Figure 4.11: Normalized tracer concentration at different times for case 4, the passive scalar was applied in a flow field obtained from a transient VOF simulation.

Figure 4.10 illustrates the transportation of the passive scalar when applied in the steady-state velocity field. The scalar quickly gets entrained into the central region of circulation (where the vortex is present when modeled with VOF) and then spreads out in a cylindrical shape. Throughout the mixing process, the highest concentration of the passive scalar remains in the center of the circulating area. The steady-state velocity field transports the passive scalar slightly faster than the transient field. In Figure 4.11, the transportation of the passive scalar when applied in the frozen transient velocity field is shown. Similar to the steady-state approach, the tracer is rapidly drawn into the vortex, but then appears to be captured there. The high concentration region is observed at the water surface and around the vortex, forming a cone-shaped area, which can be seen through the mixing process. .

The accuracy of the tracer transportation is analyzed by comparing the concentration of the tracer at the probe location against the readings from the experiment. In Figure 4.12 the mixing on the fields obtained through steady and transient simulations of case 4 are compared to one of the tests made at the second tracer location that is shown in Figure 4.9.

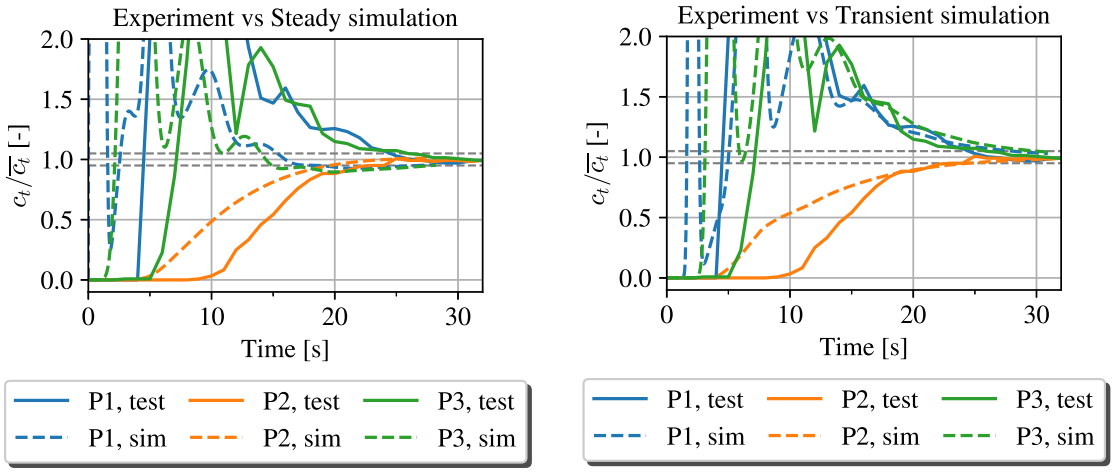

(a) Experiment compared with steady-state field.

(b) Experiment compared with transient field.

Figure 4.12: Comparison of tracer concentration at probe positions between experiment and simulation. The readings show that the mixing on the frozen field obtained with a transient simulation corresponds better with the experiment than the one obtained with steady simulation. The comparison is made for case 4

The comparison shows that the concentration calculated in the field from the transient simulation corresponds well with the experiment in terms of the trend except for the initial response. The mixing on the field from the steady simulation shows a different trend than the experiments for probes 1 and 3, indicating a low tracer concentration at the surface after 15 seconds.

4.4.3 Mixing time comparison

The mixing time for the simulations is based both on probe measurements as in the experiments and the coefficient of variance where the limit is set to $CV = 0.0283$ based on equation (2.8). The required mixing time to reach 95 % homogeneity of each case in the experiments and simulations are presented in Figure 4.13. The mixing times are rounded upward with the accuracy of one second since the sampling frequency in the experiments is 1 Hz.

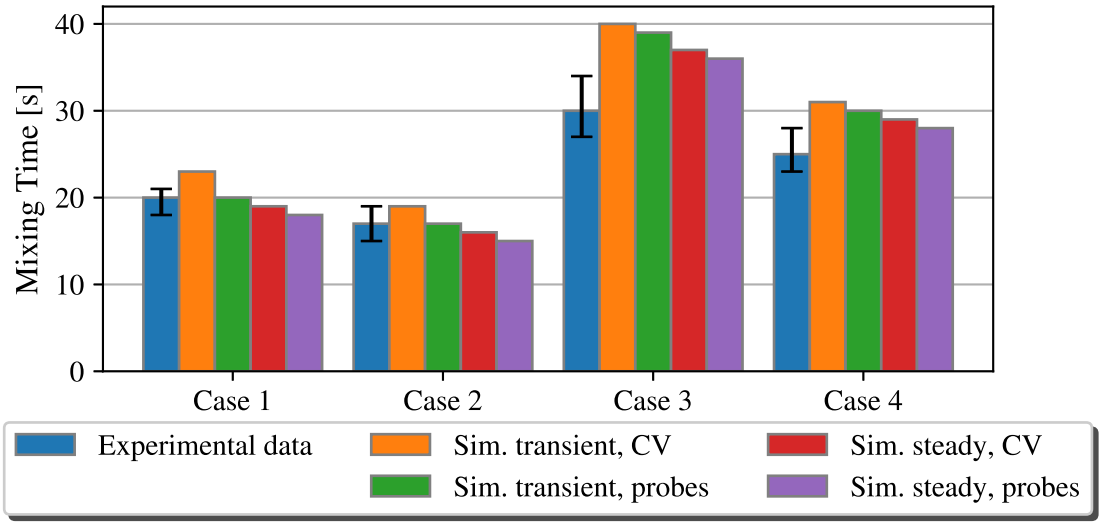

Figure 4.13: Time required to reach 95 % homogeneity in experiments and simulations. The simulation of the mixing is done on velocity fields obtained both with steady-state and transient simulations, and by measuring the concentration both with probes as the experiment and with coefficient of variance.

From Figure 4.13 it is clear that mixing where the passive scalar was added in steady-state fields consequently generates shorter mixing times than when the passive scalar was added in frozen transient fields. Moreover, mixing times based on probes measurements always give a few seconds shorter mixing times than when based on CV. However, the probe measurements consistently gives results close to CV which indicates that the probe placement is representative of the whole tank volume.

In case 1 and 2, where no vortex is present the experimental and simulation results are close to each other. In those cases, all simulation results, except the transient based on CV, are within the error bars from the experiments. In case 3 and 4 however, all simulations give an over prediction of the mixing time with 12-30 %, and only one simulation is within the error bars from the experimental results.

4.4.4 Mixing time correlations

The rule of thumb used for mixing is that the water volume should pass through the impeller four to five times to reach a homogeneous mixture of 95 %. This rule is evaluated in Figure 4.14 for the mixing times based on CV obtained from the transient simulations and by using the volumetric flow rate also obtained from the transient simulations.

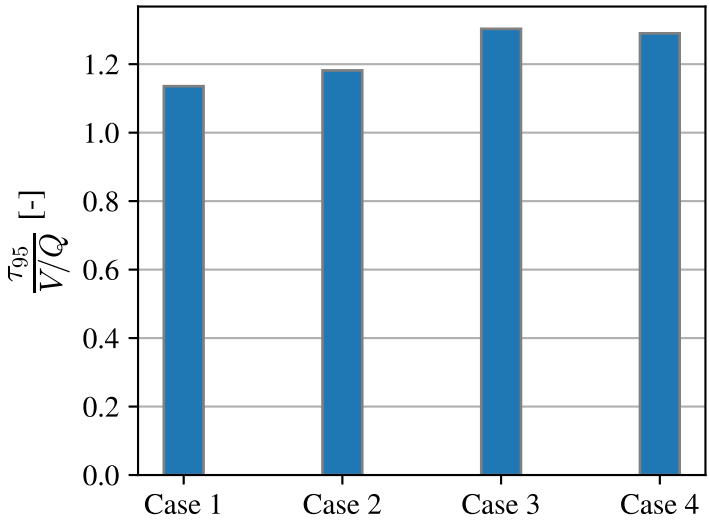

Figure 4.14: Number of turnover times necessary to reach 95 % homogeneity of the mixture. Both the mixing time and the volumetric flow rate through the impeller is obtained from the transient simulation. The mixing time is based on CV.

Based on the volumetric flow rate obtained in the simulations this rule of thumb significantly over predicts mixing times, where one to two flow through times would be more accurate. The use of turnover times however regards the change of fluid volume and shows small variation. This prediction is also practical since the pumping number, which can be used instead of the volumetric flow rate, shows relatively small variations with large changes in fluid volume. The dimensionless mixing time on the other hand is affected to a large extent when changing the water level as seen in Figure 4.15.

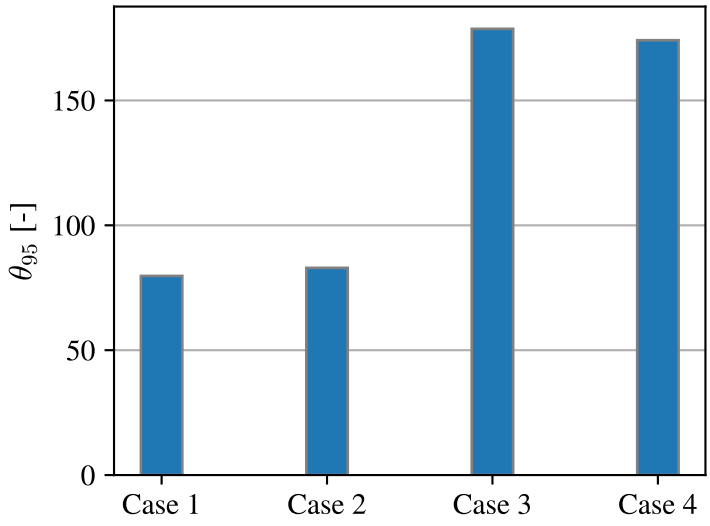

Figure 4.15: Dimensionless mixing time to reach 95 % homogeneity. The mixing time is based on CV from the transient simulations.

4.5 Simulation time

The steady-state and transient simulation approaches, both with RSM, result in significantly different computational times which should be taken into account when evaluating the methods. The transient simulations first require a steady solution for initialization and then need to reach a quasi-steady state while subject to the limitation of time step size. Regarding case 1 and 2 both the steady and transient simulation uses the same mesh as there is no vortex presence. For those cases, the transient approach increases the computational time by more than one order of magnitude compared to the steady approach. The transient simulations of case 3 and 4 uses a mesh refinement where the vortex is present and the increase in simulation time is more than two orders of magnitude.

5 Discussion and Conclusion

The purpose of this thesis was to investigate and analyze methods used to simulate a stirred tank in CFD with the focus of regarding the presence of a vortex. In the following chapter some of the results are discussed along with the methods they were obtained with. The conclusions are then presented as well as suggestions for future work that was found based on results in this thesis.

5.1 Discussion

The readings from the experiments were of the order of ~ 1 Nm, with fluctuations of an amplitude up to 0.3 Nm. The test of the torque sensor showed an accuracy of ± 0.1 Nm. Due to the low magnitude of the readings compared to the precision of the measurement instrument, the range of accuracy is around 10 % compared to the readings. That is almost the same size as the fluctuations that occurred in the experiments, which adds some uncertainty to the torque readings.

The increased power number in case 2 compared to case 1 from the experiments is a bit unexpected as the flow is fully turbulent and the power number is therefore expected to be constant as it is in the simulations. It is possible that the uncertainty in the torque readings from the experiment has an influence on this, while another possible cause is that there are physics occurring in case 2 that is not captured in the simulation. Since case 1 and 2 are simulated with a fixed water surface in both the steady-state and transient simulations the flow might behave more similarly than what actually is the case. Even though the water surface is almost flat, some fluctuations occur on the surface which appear to be chaotic and are faster and slightly larger in case 2 compared to case 1 which might contribute to more resistance in the fluid and therefore a larger power number.

The finding that RSM is the only model that could solve the vortex is interesting since the SST $k-\omega$ have been successful in previous work. Those cases however considered a center mounted impeller and the turbulence was found to be close to isotropic in the bulk flow. It is possible that the SST $k-\omega$ is unsuccessful in this thesis due to the degree of anisotropy in the flow, seen in figure 4.3. In order to investigate this further and determine if the degree of anisotropy is critical when solving the free surface, the degree of anisotropy should be compared to a case where the SST $k-\omega$ model is able to solve the free surface of the vortex.

The comparison of tracer concentration at probe positions between simulations, where the tracer was applied in fields obtained from transient simulations with a vortex, and tests, showed good correspondence in terms of the trend, except for the initial response (Figure 4.12). This discrepancy is likely due to the differing methods of tracer application in the water. In the experiments, the tracer was poured onto the water surface over a period of approximately 3 seconds. In the simulations, the total volume of the tracer was initialized all at once and applied just below the water surface.

The transport of the tracer is solved on a freezed flow field it is therefore assumed that the change of the flow field in time is small or has no impact on the mixing. The vortex was found to stabilize and this assumption may be accurate to some degree in the bulk flow. This is however not the case in the vicinity of the impeller, which obviously rotates. In Figure 4.6b and 4.11 it can be seen that the flow moves along the vortex down to and through the impeller. The movement of the impeller might therefore have some impact on the mixing of the tracer that has not been considered. Ideally it should be studied if the position of where the impeller is stopped has an impact on the mixing, as well if there is an impact on results by resolving the rotation of the impeller during mixing.

5.2 Conclusions

The required mesh resolution determined in the mesh convergence study aligns well with what has been found in previous work and the initial guess based on the literature review. The choice of RANS turbulence model did not have a significant impact on the mesh requirement. The addition of the VOF solver required the mesh to be refined in order to solve the vortex. The cell size of 2 mm where the vortex is present is found to be sufficient to resolve large features of the vortex and give converged results of power number, pumping number, and mixing time.

In cases with a vortex, it is found that the turbulence model has a significant impact on all results. The turbulence is found to not be fully isotropic and the RSM produces results more similar to DES than $k-\varepsilon$ and SST $k-\omega$. Furthermore, RSM is the only turbulence model of the three that can solve the vortex. The simulated vortex resembles the one that is present in the experiment.

For the purpose of obtaining data such as the power number, pumping number, and mixing time, steady-state simulations with a fixed water surface yield satisfactory results that are comparable to both the transient simulations and the experiments, even in cases where a vortex is present. The comparison between simulation and experimental results demonstrates good agreement regarding the power number. As for the mixing times, good agreement is observed for cases 1 and 2, while for cases 3 and 4, the mixing times are overpredicted by up to 30%. The pumping number, calculated from transient simulations where the rotation is modeled with the SM, generates values approximately 5% lower than those obtained from steady-state simulations.

The transient behavior of the mixing process agree with experiments to some extent in terms of the over all trends. The velocity field from the steady-state simulations is however different compared to transient VOF simulations when a vortex is present and therefore does not accurately model the transient behavior of the mixing process. The largest difference in transient behavior is the initial response and is likely due to the difference in how the tracer is applied to the tank between simulation and experiments.

The rule of thumb that relates mixing time to the volumetric flow rate of the impeller and water volume works well and is consistent both between different impellers speed but also different water levels. This rule is also found to be particularly useful in practice if the pumping number is used as in equation (5.1) instead of the volumetric flow rate since the variation of the pumping number is small between different impeller speeds and water volumes.

$$\tau_{95,est} = n\frac{V}{ND^3N_Q} \tag{5.1}$$

Evaluation of the mixing time rule suggest that $1 < n < 2$ gives a good estimation of the mixing time rather than four to five which has previously been used.

5.3 Future considerations

A difference in power number was found between case 1 and 2 in the experiments but not in the simulation. Possibly there is something that occurs in the experiment that is not resolved in the simulations. Even though the water surface is flat there are still small chaotic movements on the surface that increases in size and speed when the impeller speed is increased. By using VOF on cases 1 and 2, the effect of these fluctuations can be investigate better and possibly find if there is an impact on the results such as power number.

The properties of the tracer fluid in this thesis are very similar to the water it is mixed with and the effect of the tracer fluid on the water was therefore neglected. In cases when particles (or fluids) have a different density than the fluid it is mixed with there is often the problem that the particles get stuck on the bottom of the tank or on the free surface. In such cases, a vortex is needed to achieve adequate mixing. The difference in results between approaches that consider or disregard the presence of a vortex is likely to be larger for such cases, especially since the vortex was found to affect the velocity field and create suction from the free surface down to the impeller.

The rotation of the impeller is not accounted for during the transport of the tracer due to the significant computational demand it would entail to solve the flow field continuously throughout the entire mixing time. An alternative approach would be to simulate the tracer transport using a repeating sequence of flow fields captured over a few impeller rotations. This approach assumes periodicity in the flow field

rather than stationarity, which is a more reasonable assumption. Exploring this approach further could be intriguing to determine if it leads to a reduction in mixing time. However, challenges need to be addressed, such as considering the tracer's behavior when it moves outside the water domain due to changes in the free surface location between different flow fields.

Bibliography

[1] Joelle Aubin, David Fletcher, and Catherine Xuereb. "Modeling Turbulent Flow in Stirred Tanks With CFD: The Influence of the Modeling Approach, Turbulence Model and Numerical Scheme". In: *Experimental Thermal and Fluid Science* 28 (Apr. 2004). DOI: 10.1016/j.expthermflusci.2003.04.001.

[2] G. Montante et al. "Effect of the Shaft Eccentricity on the Hydrodynamics of Unbaffled Stirred Tanks". In: *Chemical Engineering Science* 61 (May 2006), pp. 2807–2814. DOI: 10.1016/j.ces.2005.09.021.

[3] Kresta Suzanne M. et al. *Advances in Industrial Mixing - A Companion to the Handbook of Industrial Mixing*. John Wiley & Sons, 2016. ISBN: 978-1-5231-0992-0.

[4] Tariq Mahmud et al. "Measurements and modelling of free-surface turbulent flows induced by a magnetic stirrer in an unbaffled stirred tank reactor". In: *Chemical Engineering Science* 64.20 (2009), pp. 4197–4209. DOI: https://doi.org/10.1016/j.ces.2009.06.059.

[5] Jennifer Haque et al. "Modelling Turbulent Flows With Free-Surface in Unbaffled Agitated Vessels". In: *Industrial & Engineering Chemistry Research - IND ENG CHEM RES* 45 (Apr. 2006), pp. 2881–2891. DOI: 10.1021/ie051021a.

[6] Bao Li et al. "Study of free-surface and solids suspension in top-sealed tanks stirred by pitched blade turbine impellers through DEM-VOF method". In: *Asia-Pacific Journal of Chemical Engineering* 17.3 (2022), e2758. DOI: https://doi.org/10.1002/apj.2758. eprint: https://onlinelibrary.wiley.com/doi/pdf/10.1002/apj.2758.

[7] Caroline Olofsson and Emma Sundell. *CFD Simulations of Mixing using a Magnetically Driven Impeller*. 2018. URL: https://hdl.handle.net/20.500.12380/256474.

[8] H. Hartmann, J. J. Derksen, and H. E. A. van den Akker. "Mixing times in a turbulent stirred tank by means of LES." In: *AIChE Journal* 52.11 (2006), pp. 3696–3706. DOI: 10.1002/aic.10997.

[9] Fengling Yang, Shenjie Zhou, and Guichao Wang. "Detached eddy simulation of the liquid mixing in stirred tanks". In: *Computers & Fluids* 64 (2012), pp. 74–82. ISSN: 0045-7930. DOI: https://doi.org/10.1016/j.compfluid.2012.05.005.

[10] Graeme L. Lane. "Improving the accuracy of CFD predictions of turbulence in a tank stirred by a hydrofoil impeller". In: *Chemical Engineering Science* 169 (2017), pp. 188–211. DOI: https://doi.org/10.1016/j.ces.2017.03.061.

[11] Fengling Yang, Shenjie Zhou, and Cuixun Zhang. "Free-Surface Turbulent Flow in an Eccentric Stirred Tank". In: *Chemical Engineering and Technology* 40.3 (Dec. 2016), pp. 561–570. DOI: 10.1002/ceat.201600354.

[12] Edward L. Paul et al. *Handbook of Industrial Mixing*. 1st ed. John Wiley & Sons, 2003. ISBN: 9780471451440.

[13] David F. Fletcher Harminder Singh and Justin J. Nijdam. "An assessment of different turbulence models for predicting flow in a baffled tank stirred with a Rushton turbine." In: *Chemical Engineering Science* 66.23 (2011), pp. 5976–5988. DOI: 10.1016/j.ces.2011.08.018.

[14] L. Davidsson. *Fluid mechanics, turbulent flow and turbulence modeling*. Göteborg, Sweden: Chalmers University of Technology [Online]. 2023. URL: http://www.tfd.chalmers.se/~lada/postscript_files/solids-and-fluids_turbulent-flow_turbulence-modelling.pdf.

[15] *Simcenter™ STAR-CCM+™ software*. 2020. URL: https://docs.sw.siemens.com/documentation/external/PL20191230144651718/en-US/userManual/userGuide/html/index.html#page/STARCCMP%5C%2FGUID-ADFCC925-E117-4630-8D86-13C171962405.html%5C%23.

[16] Tsan-Hsing Shih et al. "A new $k-\varepsilon$ eddy viscosity model for high reynolds number turbulent flows". In: *Computers & Fluids* 24.3 (1995), pp. 227–238. DOI: https://doi.org/10.1016/0045-7930(94)00032-T.

[17] Yacine Addad et al. "Optimal Unstructured Meshing for Large Eddy Simulations". In: *Quality and Reliability of Large-Eddy Simulations* 12 (Jan. 2008). DOI: 10.1007/978-1-4020-8578-9_8.

[18] Horiba. *Measuring Salinity of Water*. 2016. URL: https://www.horiba.com/int/water-quality/applications/water-wastewater/measuring-salinity-of-water/ (visited on 2023-06-13).

A Experimental conductivity measurements

A.1 Water level 408mm and impeller speed 208rpm.

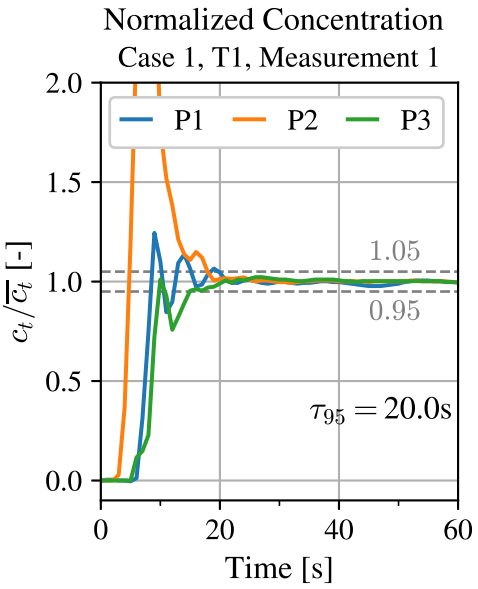

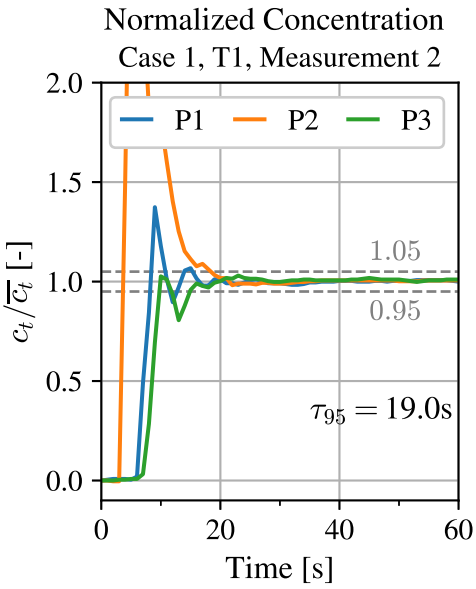

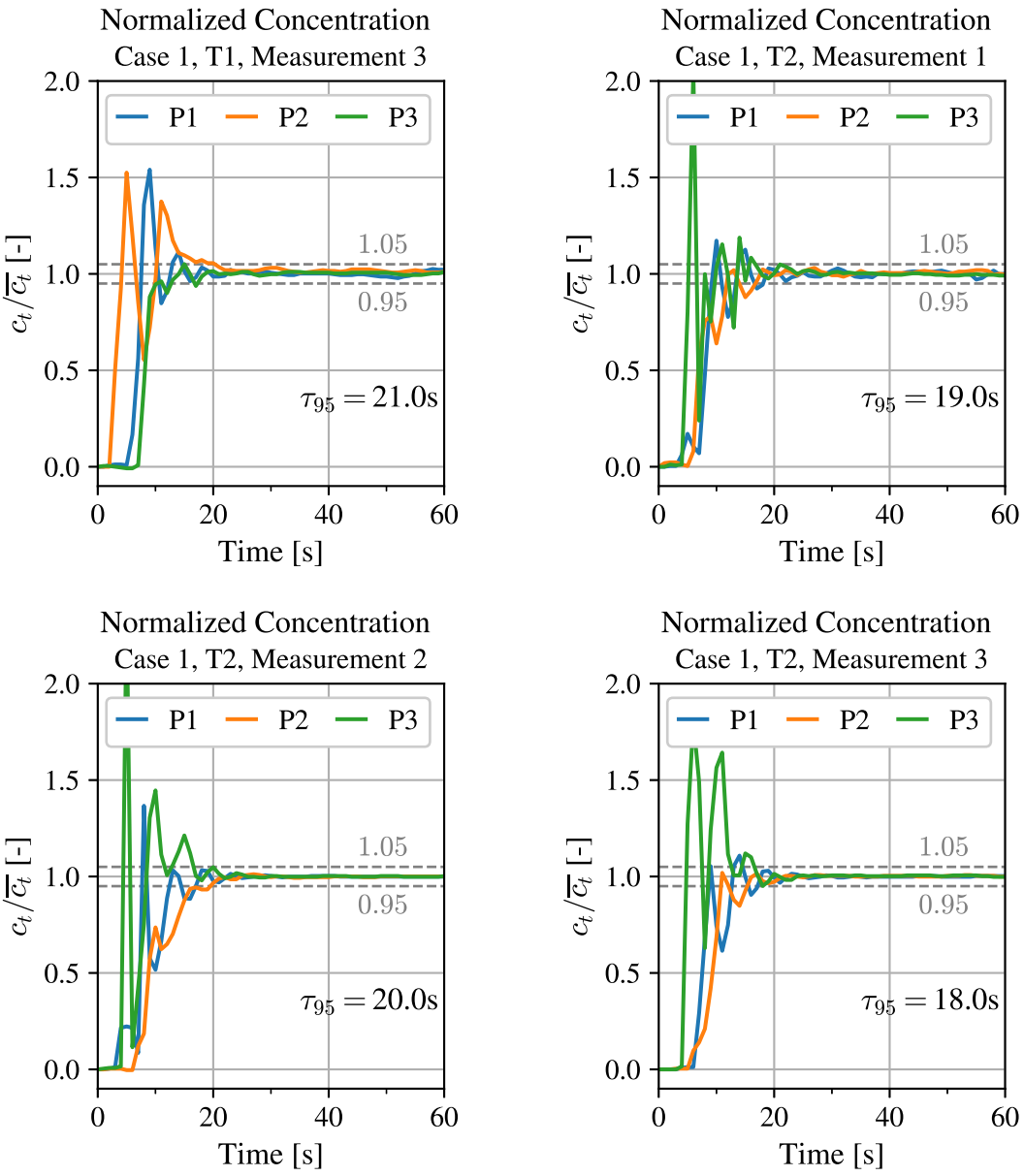

Figure A.1: Measurements with a water level of 408mm and an impeller speed of 208rpm.

A.2 Water level 408mm and impeller speed 262rpm.

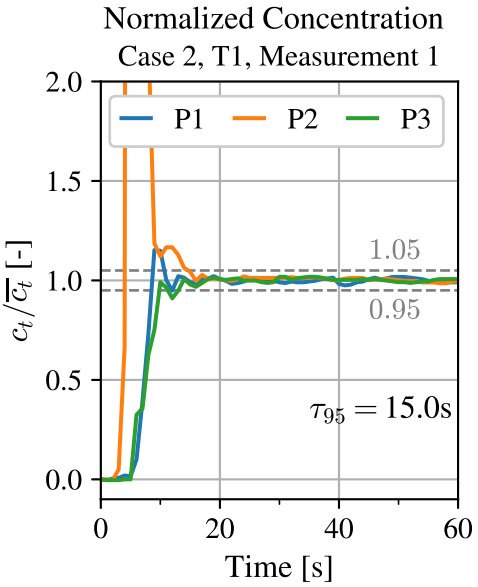

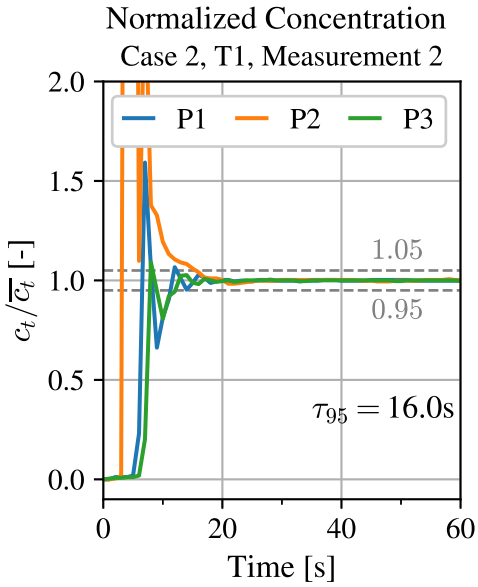

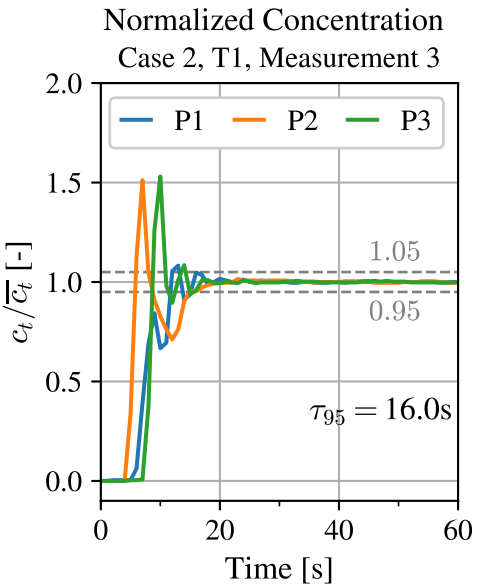

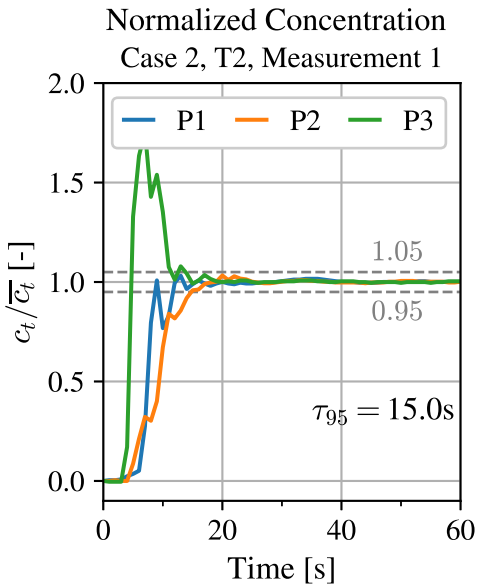

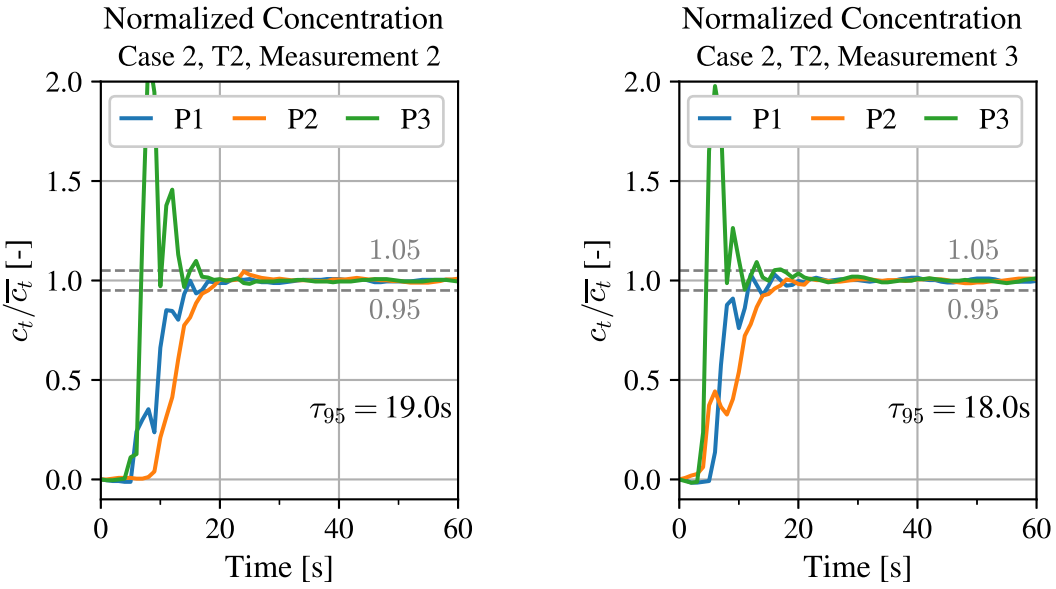

Figure A.2: Measurements with a water level of 408mm and an impeller speed of 262rpm.

A.3 Water level 816mm and impeller speed 268rpm.

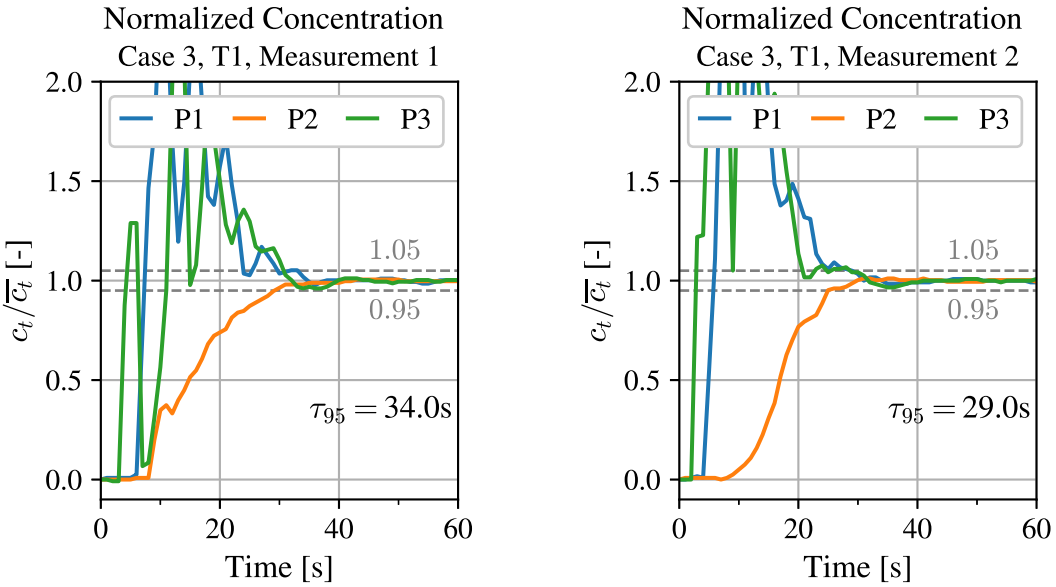

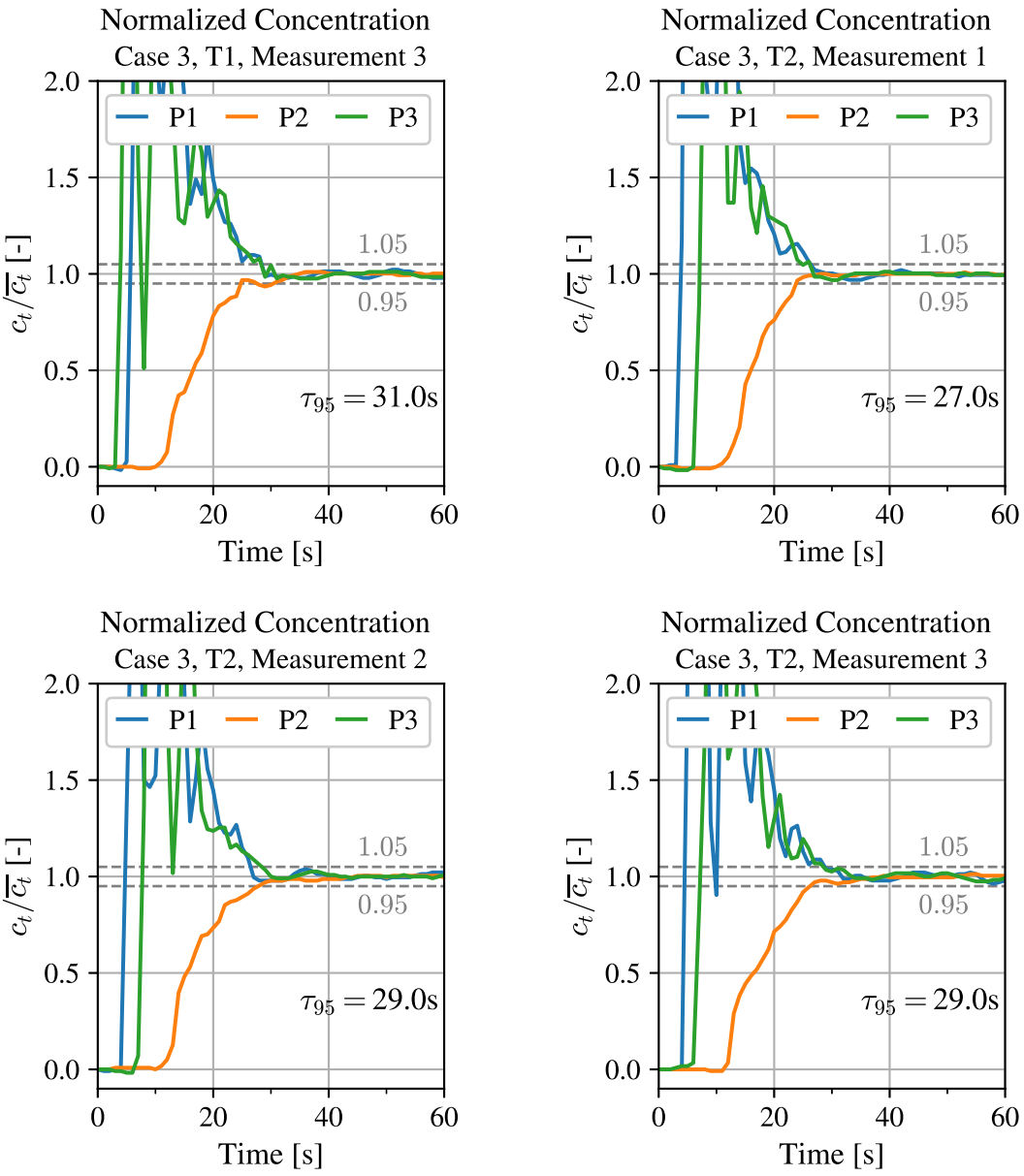

Figure A.3: Measurements with a water level of 816mm and an impeller speed of 268rpm.

A.4 Water level 816mm and impeller speed 337rpm.

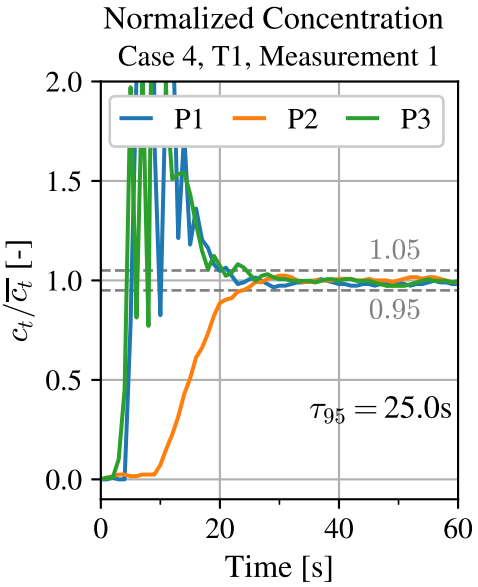

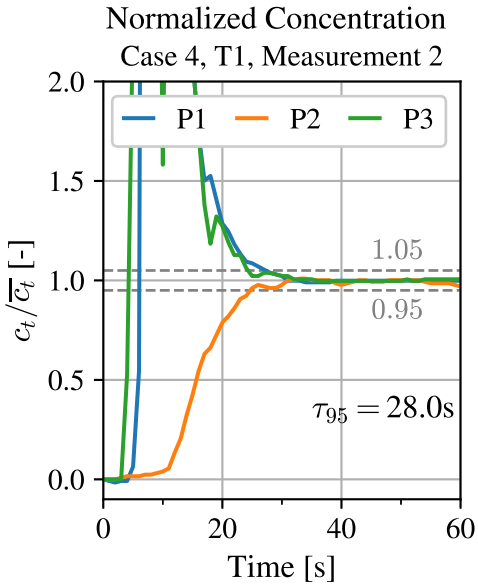

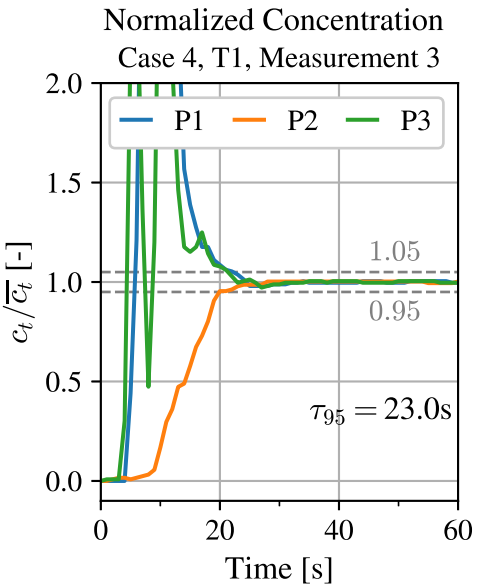

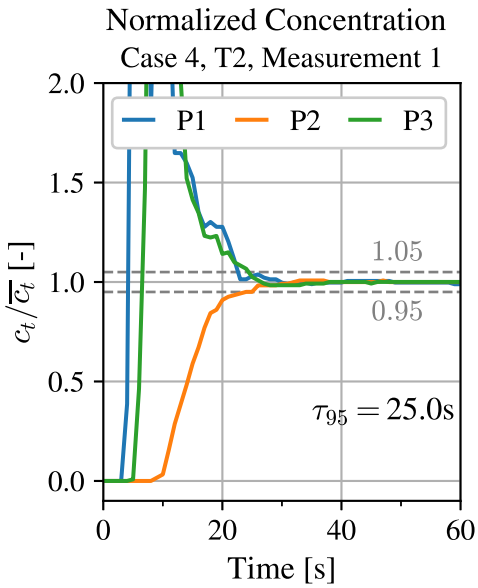

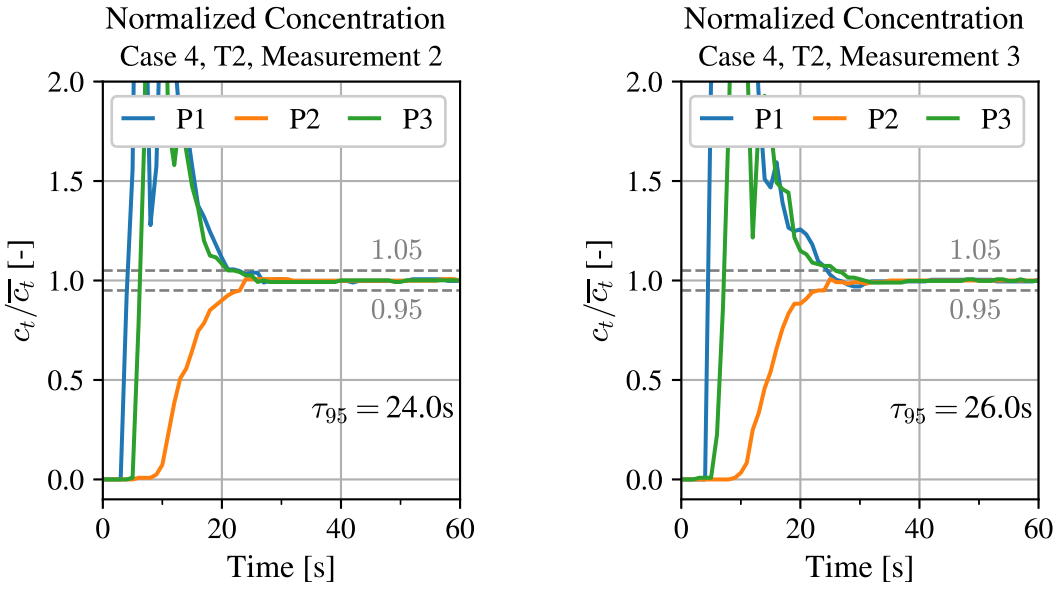

Figure A.4: Measurements with a water level of 816mm and an impeller speed of 337rpm.

A.5 Water level 816mm and impeller speed 337rpm, double amount of tracer liquid.

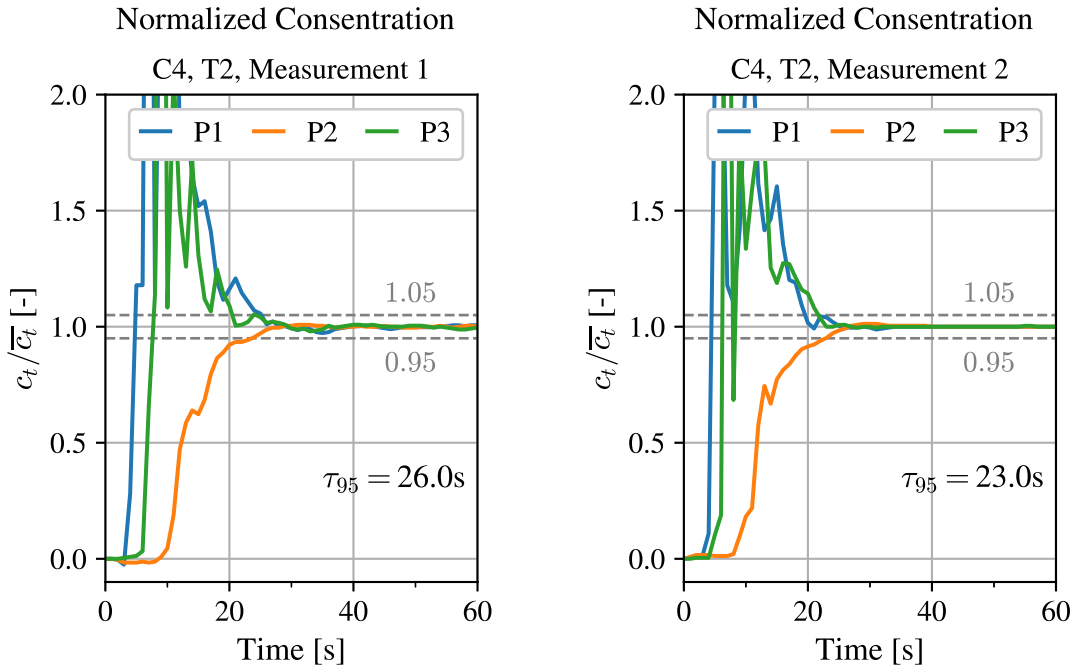

Figure A.5: Measurements with 200g saline, a water level of 816mm and an impeller speed of 337rpm.

B Transport of the passive scalar

The spread of the passive scalar over time. The normalized tracer concentration is shown at different times for the four cases, applied both in the steady flow field and in the frozen transient flow field.

B.1 Case 1

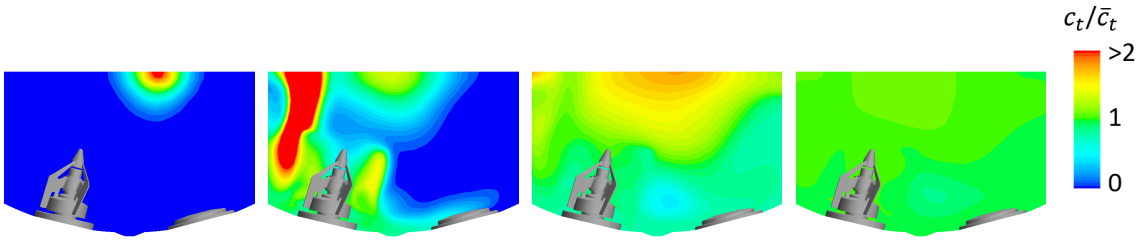

(a) 1 s (b) 4 s (c) 8 s (d) 15 s

Figure B.1: Passive scalar applied in the steady flow field.

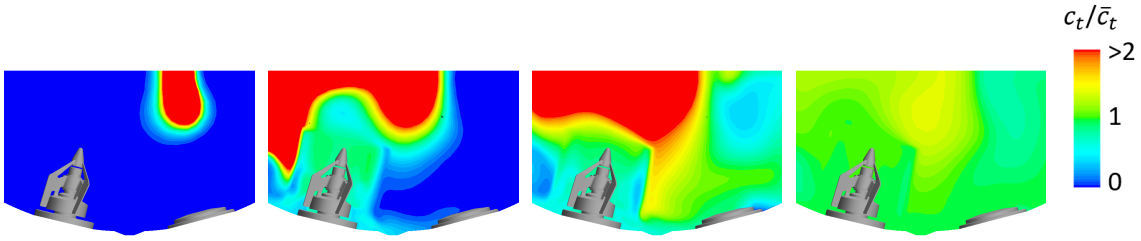

(a) 1 s (b) 4 s (c) 8 s (d) 15 s

Figure B.2: Passive scalar applied in the frozen transient flow field.

B.2 Case 2

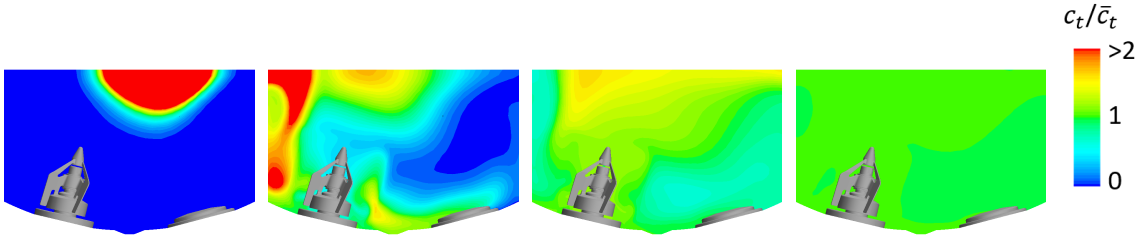

(a) 1 s (b) 4 s (c) 8 s (d) 15 s

Figure B.3: Passive scalar applied in the steady flow field.

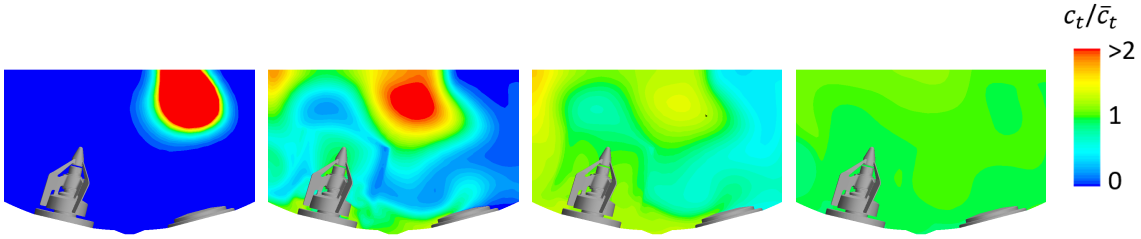

(a) 1 s (b) 4 s (c) 8 s (d) 15 s

Figure B.4: Passive scalar applied in the frozen transient flow field.

B.3 Case 3

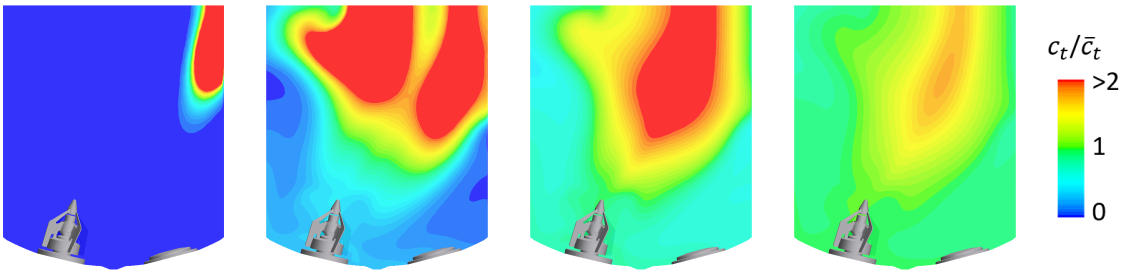

(a) 2 s (b) 10 s (c) 18 s (d) 25 s

Figure B.5: Passive scalar applied in a flow field obtained from a steady simulation with locked water surface.

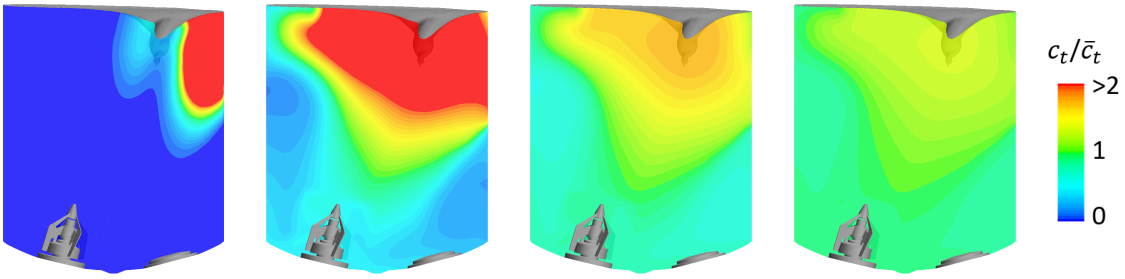

(a) 2 s (b) 10 s (c) 18 s (d) 25 s

Figure B.6: Passive scalar applied in a frozen flow field obtained from a transient VOF simulation.

DEPARTMENT OF MECHANICAL AND MARITIME SCIENCE
CHALMERS UNIVERSITY OF TECHNOLOGY
Gothenburg, Sweden
www.chalmers.se

CHALMERS
UNIVERSITY OF TECHNOLOGY